Characterization of Surface Urban Heat Island in the Greater Toronto Area Using Thermal Infrared Satellite Imagery

by

Minjie Wang

A thesis
presented to the University of Waterloo
in fulfilment of the
thesis requirement for the degree of
Master of Science
in
Geography

Waterloo, Ontario, Canada, 2015

Author's Declaration

I hereby declare that I am the sole author of this thesis. This is a true copy of the thesis, including any required final revisions, as accepted by my examiners.

I understand that my thesis may be made electronically available to the public.

Abstract

For the past decades, there have been increasing concerns about urban environmental degradation, especially under the circumstance of urbanization. This thesis compares the trends between air temperature and surface temperature, and characterizes spatial distribution and connection with relevant urban characteristics, in the Greater Toronto Area (GTA) of Ontario in the context of surface urban heat island (SUHI). The trends in annual and seasonal temperature were investigated in the GTA from 1984 to 2014. The Mann-Kendall test is used to assess the significance of the trends and the Theil-Sen slope estimator is used to identify their magnitude. Statistically significant increasing trends for annual mean temperatures are observed mainly at the urban and suburban stations. The temperature variation is consistent with the pace of urbanization, however, the choice of the stations is vital in the estimation of the UHI intensity which can overestimate or underestimate the prediction. A local scale investigation was continued by applying Landsat and ASTER thermal-band images in order to characterize SUHI intensity in the study area. Results show that strong SUHI phenomenon is mainly observed at downtown Toronto and industrial areas. As the enhancement of urbanization, tracking and monitoring of SUHI is imperative to understand the potential impact of the increased heat waves.

Acknowledgements

First of all, I would like to express the deepest appreciation to my supervisor, Professor Dr. Jonathan Li, who continually and persuasively conveys a spirit of adventure in regard to research. Without his genuine guidance and continuous support, this thesis would not have been possible. I would also like to thank my thesis examining committee members, Dr. Jane Law with the School of Planning, Dr. Chris Fletcher and Dr. Su-Ying Tan, both with the Department of Geography and Environmental Management, for the valuable time they shared in providing constructive comments and valuable suggestions.

I would also like to extend my sincere thanks to all the faculty and staff members in the Department of Geography and Environmental Management for their guidance and countless help throughout my coursework and completion of my thesis. Thanks also go to my graduate student fellows for making my experience in graduate school one of the most enjoyable.

Last but not least, my deepest gratitude goes to my parents and my wife for providing a tremendous wealth of unconditional love and sincere support.

Dedications

To My Greatest Parents, Jian Wang and Xinsu Lai,

&

To the Love of My Life, Yi Zheng

Table of Contents

List of Figures

List of Tables

List of Abbreviations

AATSR: Advanced Along-Track Scanning Radiometer

ACPC: Atmospheric Correction Parameter Calculator

ARIMA: Autoregressive and Integrated Moving Average

ASTER: Advanced Spaceborne Thermal Emission and Reflection Radiometer

AT: Air Temperature

ATLAS: Advanced Thermal and Land Applications Sensor

BLHI: Boundary Layer Heat Island

CLHI: Canopy Layer Heat Island

CMA: Census Metropolitan Area

CNE: Canadian National Exhibition

DN: Digital Number

EC: Environment Canada

EPA: Environmental Protection Agency

ET: Evapotranspiration

ETM+: Enhanced Thematic Mapper Plus

GCS: Geographic Coordinate Systems

GOES: Geostationary Environmental Satellite

GTA: Greater Toronto Area

IPCC: Intergovernmental Panel on Climate Change

LDCM: Landsat Data Continuity Mission

LST: Land Surface Temperature

LULC: Land Use and Land Cover

MK: Mann-Kendall

MODIS: Moderate Resolution Imaging Spectroradiometer

MW: Mann-Whitney

NAD: North American Datum

NDVI: Normalized Difference Vegetation Index

NOAA: National Oceanic and Atmospheric Administration

OLI: Operational Land Imager

SHI: Surface Heat Island

SLC: Scan Line Corrector

SNR: Signal-to-Noise

SUHI: Surface Urban Heat Island

SVF: Sky View Factor

SWIR: Short Wave Infrared

TIRS: Thermal Infrared Sensor

TIROS: Television Infrared Observation Satellite

TM: Thematic Mapper

ToA_r: Top of Atmosphere Radiance

TSA: Theil-Sen Approach

UHI: Urban Heat Island

USGS: US Geological Survey

VNIR: Visible and Near Infrared

Chapter 1

Introduction

1.1 Background

There are two terms are frequently introduced in previous journal articles when studying urban environmental phenomenon. The first one is urban heat island (UHI) which compares the air temperature (AT) data from weather stations inside and outside urban area. The other one is surface urban heat island (SUHI) which exams the difference of land surface temperature (LST) derived from remote-sensing data (Sobrino et al., 2013). In this article, the main focus is put on the SUHI while the UHI will also be presented as supplementary information.

The study of urban scale temperature focuses on three different layers as shown in Figure 1.1 which are surface layer, canopy layer and urban boundary layer. Surface layer refers to the ground surfaces which is the lowest layer contact directly with the atmosphere. The surface layer is the warmest part in the system as most of solar heat is absorbed by this layer (Oke, 1978). Canopy layer indicates the portion between the surface layer and upper bound of urban dwellings. Different with the surface layer, the canopy layer is where majority of heat transferred. The urban boundary layer, which changes its thickness from more than 1 km at daytime to hundreds of meters or less at night, is the atmosphere part above that interacted with the canopy layer. Compared with the surface layer and the canopy layer, the urban boundary layer is more stable as energy transferred to this layer is equally distributed at a meso-scale (Arnfield, 2003). Accordingly, there are three types of UHIs which are surface heat island (SHI), canopy layer heat island (CLHI) and boundary layer heat island (BLHI). The CLHI refers to UHI whereas the SHI refers to SUHI in this thesis.

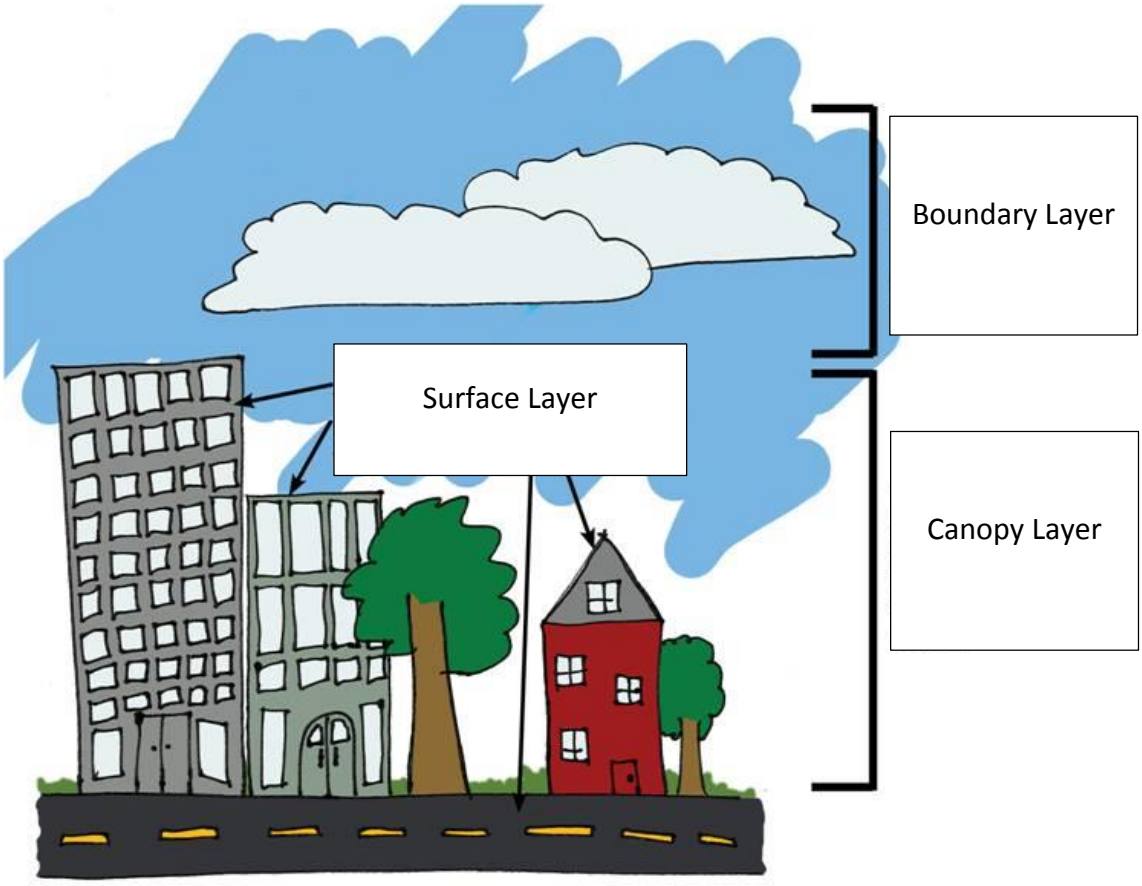

Figure 1.1 Urban Heat Island Layers
(Source: U.S. Environmental Protection Agency (EPA), 2008)

A developed region presenting higher atmospheric temperatures than circumjacent rural areas uninfluenced by human interference is called an Urban Heat Island (UHI) which was first investigated and described in the early 1800s by Howard (1833). It has become increasingly recognized by people that large construction and development imperils the climate within the adjacent region (Memon et al., 2009; Taha, 1997). Increasing anthropogenic change in urbanization process can lead to inadvertent climate modifications in urban areas (Lo, 1997). For instance, urban canyon effect, where surfaces of skyscrapers generate hot waves that have been absorbed from heating in the daytime during the night will intensify the UHI. Also high buildings

decrease the sky view factor (SVF) and hence increase the magnitude of the UHI by weakening longwave radiation emission rate (Oke, 1982). Besides the limitation of longwave energy emission from urban surface, the canyon between high buildings promotes the chance for shortwave radiation to be reabsorbed by decreasing in albedo. During the process of urbanization, vegetated areas are replaced with impervious artificial surface. Urban surface is exposed under sunlight to absorb and store radiation during the daytime. Urban surface will then transfer the stored energy to the air throughout the evening. For moist urban surface areas which are covered by dense vegetation, latent heat transfer is happened between the urban surface and the atmosphere. Latent heat transfer does not change the temperature during the exchange of energy within the energy balance cycle. Water part of the urban surface also reduce the intensity of UHI by evaporation. However, impervious surfaces replace the original vegetative portion and reduce the humidity content of the urban. It leads to direct sensible heat transfer of energy by radiation which promotes the UHI. Typically, higher concentrations of impervious surfaces in urban cores (Xian & Crane, 2006) can absorb 80% to 95% solar flux in US cities with an average surface albedo of 0.15 to 0.2 (Taha, 1997).

In the meantime, urban geometry "texture" has been modified by high rise and high density development. Urban geometry, namely the plan of building placement and street arrangement are functional and aesthetic driven before. As the intensification of UHI in urban areas, scholars start to investigate the impact from unconscionable urban planning. Besides the modification of urban surface and shape, appendages of urbanization could include high demand of energy from electric power, transportation (Taha et al., 1999) and air pollution (Stone, 2005). Such kind of transformation leads to additional alterations of local environment. Landsberg (1970) found that

decreasing of wind speed as well as reduction of urban surfaces albedo presented within developed urban areas. The potential decrease in albedo of 20% was calculated in Craig and Lowry (1972). Lower albedos in urban and suburban areas than rural areas have been proved by aerial measurements (Christen & Vogt, 2004). The relationship between urban albedo and the UHI has been explored and modeled which points out that residential areas have lower albedo compared with city core (Sailor & Fan, 2002) and snowfall in high latitude cities can highlight the differential of urban/rural albedo (Oke, 1988).

UHI will also intensify heat rejection from residential and commercial sections by derived demand of air conditioner during hot day and night with a temperature raising of 0.5℃ at street level (Salamanca et al., 2014; Tremeac et al., 2012). As a result, urban areas receive additional anthropogenic heat from human activities which do not apply to rural areas. The primary source of the heat comes from building use heating (or cooling) and transportation (Sailor & Lu, 2004). Tokyo, as one of the international metropolis, energy release in urban core can reach as high as 1590W/m^2 in winter morning working hours (Ichinose 1999). With larger city scales in North America, the anthropogenic heat is still significant but more diffuse. Sailor and Hart (2006) calculate the citywide average anthropogenic heat release at New York City in the winter. The value fluctuate between 85 to 96 W/m^2. Anthropogenic heat scale changes within yearly cycle as heating needs in winter and cooling needs in summer. In addition, energy use depends on latitude driven heating or cooling situation preference. The additional heat generation creates a vicious circle and has additive effects as severe UHI. Another effect resulted from UHI is the increasing of greenhouse gas as it has been shown to scale with temperature (Stone, 2005).

As one of the two major factors governing the near surface urban heat island, the weather and

climate conditions can have impacts on the generation of the UHI, in some cases, contribute or eliminate it (Landsberg, 1981). Widely acknowledged weather factors, which are less cloud cover and reduced winds, tend to exacerbate the UHI development (Arnfield, 2003; Morris, 2000). Oke (1987) found that wind speed is influenced by the value of surface roughness and the heat island intensity decreases with enhanced wind speed. Voogt and Oke (2003) demonstrated that increasing cloud will reduce radiative cooling at night and also reduce the heat island. Furthermore, local scale climate might also contribute to UHI. There is evidence that large water bodies could influence the local weather nearby (Kusaka et al., 2000). The local scale climate of the GTA is fluctuated by a change in elevation from the shore of Lake Ontario. This kind of topography will cause slope winds during the night or subsidence heating when a strong northeast temperature gradient appears (Munn et al., 1969). Generally, Lake Ontario will moderate the summer extreme temperature, which is the "Lake Breeze" effect, by blowing winds from water to land (Scott and Huff, 1996). Additional factors such as the scattered and emitted radiation from atmospheric pollutants to the urban area, the production of greenhouse gas and aerosol concentrations from air conditioning and refrigeration systems, as well from industrial processes and motorized vehicular traffic, have been recognized as additional anthropogenic climate factors for the UHI. However, the limitation of data regarding to historical records of the study area restricts the possibility of interpreting UHI from weather and climate factors.

Another major factor in the development of a UHI is the conversion of rural lands to urban lands with impervious surfaces and sparse vegetation. Urbanization, whether in the form of residential, commercial, or industrial, influences the UHI through the change of land use and land cover. This shift results in less canopy and moisture to keep urban areas cool. Vegetation coverage plays a very

important role in the study of UHI by introducing the evapotranspiration (ET) rate. The situation could be totally different between forested regions and arid regions. Relative high vegetation coverage in rural area of forested regions leads to stronger UHI by increasing the temperature difference (Imhoff et al., 2010). However, more vegetation (parks and lawns) in urban area of arid regions makes the urban cooler than surrounding rural desert (Brazel et al., 2000).

The researches of UHI carried on in the early years mainly use the meteorological data from fixed thermometer networks (i.e., ground-based weather stations). Thermometers at ground-based weather stations measure the air temperatures at high temporal resolution with a long recording period, but at poor spatial resolution. Plenty, evenly distributed stations would be necessary to generate an accurate thermal map of a city. Besides, weather stations have high upkeep cost and setting cost. The change of surrounding environment near weather stations will also affect the accuracy of long term recording data. However, there is no denying that historical meteorological data plays a very important role in studying UHI phenomenon. By examining long term annual mean temperature in the GTA, it is found that the increasing trend of temperature is consistent with the pace of urbanization which starts from 1920 at downtown Toronto and 1960 at the suburban areas (Mohsin & Gough, 2014). By looking for UHI effect on the temperature trends of several American cities, Stone (2007) suggests that the temperature trends between urban stations and rural stations is clearly different. Studies are also conducted in Asia, for example, in the city of Ankara, Turkey. The effect of the UHI on diurnal temperature variation is most pronounced in winter (Çiçek & Doğa, 2006).

As the development of satellite remote sensing, studies have been shifted to explore SUHI by

measurements of surface temperature over large areas of urban cities due to more spatial coverage with respect to ground-based observations (Fabrizi et al., 2010). The assessment of SUHI using satellite remote sensing data is firstly proposed by Rao (1972). Followed by a wide range of researches offering improvements over their ancestors, remotely sensed thermal infrared (TIR) data have been widely applied to studies of urban thermal environment and dynamics (Weng, 2009). While satellite data analysis provides useful information, it is restricted in three aspects. First, over flight times of satellite platforms are usually at a certain time of a day which provide no coverage during the whole day. Second, LST recorded by the satellites do not reflect the air temperature directly. Third, the temporal frequency of imaging by satellite platforms ranges from every 2 to 16 days, assuming clear sky conditions, limits the available data that can be processed. Previous studies regarding to the "satellite-derived" SUHI will be illustrated in next chapter detailedly.

There are increasing concerns about the side effect of UHI regarding to our urban environments, especially how abnormal temperature will interact with the UHI (Coutts et al., 2010). The leading consequences from UHI are high morbidity and mortality caused by urban heat wave (Smargiassi et al., 2008; Curriero et al., 2002). Extreme heat will lead to various pathogenic condition such as heat stroke, heat cramps, dehydration and heat-related mortality. Thousands of people died of heat every year all over the world (Keatinge et al., 2000; Loughnan et al., 2010). In 2003, heat waves affected France and resulted in more than 15000 deaths which was part of total 70000 people died across the whole European (Fouillet et al., 2006). Similar tragedy happened in Chicago, USA in 1995 and killed 739 excess people (Whitman et al., 1997). During the heat wave, heat stroke counts a big portion of total patients and it will continue to threat residents' health for the following years

(Argaud et al., 2007). Inhabitants with chronic disorders and the elder are more susceptible to UHI (Semenza et al., 1996). UHI also increases the development of photochemical smog which results from evaporation and mixing of pollutants from urban surface (Rosenfeld et al., 1995). Constantly strengthen of extreme weather and climate events by UHI could become serious challenges for socioeconomic and natural systems. More serious UHI means more energy consumption as cooling system needs to work more frequently in order to keep indoor optimal temperature. Parks in the city help to mitigate urban temperature by 1.5˚C within a distance of 2 km from the park witch equals to 4000 kWh of electricity used to run air conditioners (Ca et al., 1998). Payton et al. (2008) estimated the loss from another view which indicated that UHIs affect the real estate value. UHI can bring atrocious local weather by increasing rainfall intensity and changing wind patterns (Dixon & Mote, 2003). UHIs also damage the ecosystems and wildlife near the urban boundary which cause more forest fire and animal extinction (Diaz et al., 2009). Another huge concern is the pollution of drinking water due to thermal pollution. Rain water runs over impervious surface instead of soaking into the ground and then collects heat, dust and toxic substances before dumping into rivers (Krause et al., 2004; Finkenbine et al., 2000).

With an increasing growth in the quantity and intensity of extreme heat events, and 80% of Canadians living in urban areas, for example, the Greater Toronto Area (GTA), Ontario, Canada, there is an urgent requirement of UHI/SUHI mapping and monitoring in spite of Canada's well-known cold temperature. In a case study of 11 North American urban areas, Curriero et al. (2002) concluded that heat related mortality increases correlatively with latitude. The possible explanation for this situation is the lack of preparatory work in northern cities for heat events, such as incomplete air conditioning in low-income apartments or insufficiency of community cooling

centres. The lack of suitable policies could be an important reason for urban environment deterioration in the GTA. How do the land use and land cover (LULC) shape the urban thermal distribution? Is there any method can be used to monitor and analyze the UHI? Is there any new emerging hot area during the past decades? To answer these questions makes it necessary and essential to translate and advance the knowledge of SUHI and UHI.

In order to solve issues caused by UHI, the first step is to explore and describe the urban environment in a full range which requires UHI monitoring and modelling. "Quantitative information on the types and distribution of the urban thermal environment can be of value in the design of cities, in engineering urban hydrologic systems, in planning for the efficient removal of air pollutants, and in assuring the success of studies of inadvertent weather modification by urbanization" (Morgan et al., 1977). Many aspects of temperature differences between urban and rural have been quantified by previous studies (Munn et al. 1969; Oke, 1973; Oke and Maxwell, 1975; Oke, 1982; Oke, 1988; Camilloni and Barros, 1997; Runnalls and Oke, 2000). However, similar studies were seldom conducted in the GTA. Therefore, this thesis explores the UHI from the role of urban development and characterizes the SUHI in the Greater Toronto Area, Ontario, Canada, by using thermal infrared (TIR) remote sensing data from the past 30 years.

1.2 Objectives of the Study

This study will mainly characterize SUHI by using LANDSAT and ASTAR imagers to observe distribution of the GTA's vegetation, land use, population and road network in relation to LST in the past years. This is accomplished using thermal band images acquired in July or August from 1984 to 2014 with good atmospheric conditions.

The specific objectives of the thesis are:

- To describe the trends of annual mean air temperature in the GTA from 1984 to 2014;
- To describe the annual and seasonal UHI intensity in downtown Toronto from 1984 to 2014;
- To compare calculated LST with historical air temperature;
- To map and characterize the SUHI intensity according to urban characteristics in the GTA;

1.3 Structure of the Thesis

This thesis consists of 6 chapters. The rest of the thesis is organized as follows:

Chapter 2 gives an introduction to the relationship between SUHI and UHI phenomenon with emphasis on mechanism and characteristics. This chapter also reviews previous studies regarding to SUHI which are conducted at different cities with different spatial, spectral and temporal scales.

Chapter 3 describes properties of the study area and summarizes the data used in this study.

Chapter 4 presents an integrated method which combines the ground station data and remote sensing data to characterize UHI and SUHI intensity graphically and numerically.

Chapter 5 presents the major results derived with different datasets by using the proposed method. Thematic maps are generated to visualize the SUHI based on different urban parameter.

Chapter 6 summarizes major findings and their implications and also suggests improvement for future study.

Chapter 2

Literature Review

2.1 Difference between SUHI and UHI

The mechanisms that contribute to the formation of UHI and SUHI are different (Peng et al., 2012). In general, the leading cause of UHI is the difference in radiative cooling rate between urban and rural areas at night while SUHI is mainly driven by the difference in radiative surface heating during the daytime inside and outside the urban area. Consequently, the variations of UHI and SUHI in spatial distribution and temporal pattern can be different (Hung et al., 2006; Voogt & Oke, 2003). Additionally, according to United States Environmental Protection Agency report (EPA, 2008), LST has indirect, but significant, influence on air temperature, particularly between the layer of urban surface and the tree canopy. Therefore, comparing of LST and AT can provide some clue for the relation between SUHI and UHI. However, the relationship between the LST and AT is not obvious and constant. LST usually varies depends on surface materials sensitively, but AT does not change at the same pace (EPA, 2008). Regardless of the lack of universal and precise transfer function between LST and AT (Nichol, 1994), the study of SUHI by looking for LST is still important because it not only helps determining the thermal behaviors in urban areas, but also helps to characterize and quantify the UHI (Weng, 2009).

2.2 Features of SUHI and UHI

Researchers have identified some common features of UHI after studying various urban climates over the years. The UHI gives a sign by gradually increased minimum, maximum and average air temperatures (Karl et al., 1988). One of the primary features of the UHI is that it presents higher intensity during the night when compared with daytime cases (Karl et al., 1988). This phenomenon

is also noted in other studies (Holmer et al., 2007; Oke, 1982) which find a sudden increase in the UHI intensity around sunset and a drop near sunrise.

Beyond that, the UHI has potential connection with population, which is another prominent feature of the UHI. Karl et al. (1988) developed a population-based regression model to calculate the UHI magnitude in the United States cities and indicated that the UHI enhanced with population by the power of 0.45 from towns to cities. Even through different rates are observed around the world, the UHI magnitude keeps positive trend regarding to the population (Oke, 1982; Park, 1986). Base on Arnfield (2003), the strongest UHI is during warm half of the year, while other study comments that it is during the hottest period of the year (Souch and Grimmond, 2006). Therefore, with plenty research results giving divergent views, it remains impossible to conclude the seasonal variability pattern of the UHI due to the complex urban environment. The strength of UHI could be uneven within a city as the physiognomy varies. For instance, highly developed areas and less vegetated regions usually experience higher temperature. An urban temperature difference of 2˚C was monitored in New York City between different weather stations within the city (Gaffin et al., 2008).

For the features of SUHI, the temporal variation pattern could be quite different from or even opposite to that of UHI which SUHI reaches maximum at noon but drops to minimum during the night (Choi et al., 2014). The maximum value of SUHI usually occurs some hours after the recorded maximum UHI according to case study in the city of Madrid, Spain (Sobrino et al., 2013). As SUHI is calculated based on LST, the SUHI is sensitive to factors which determine the LST, for instance, physical properties of urban surfaces, street geometry, human activities, LULC, vegetation indices and traffic volume (Weng, 2009).

2.3 SUHI and UHI Studies

2.3.1 Energy Balance Approach

In order to describe UHI and urban thermal behavior, principle of urban surface energy balance is fundamental. Oak (1982) introduced the following equation (Eq. 2-1) to present the net surface radiative flux density (Q^*).

$$Q^* + Q_f = \Delta Q_s + Q_e + Q_h \quad (2\text{-}1)$$

where Q^* is principally contributed by short-wave and long-wave radiation fluxes from day and night, Q_f is the anthropogenic heat flux that is added to show heat generated by human activities or vehicles, ΔQ_s is the surface heat storage that is heat transferred by the conduction into the ground or high-rises, Q_e is the turbulent latent heat showing flow of heat exchanged during the change of state of the water, Q_h is the turbulent sensible heat showing the flux of heat interflowing between object surfaces to the atmosphere during temperature change. The latest development and application of energy balance approach were reviewed by Grimmond (2006) which highlighted the role of in situ measurements using tower-based heat fluxes monitoring equipment. However, a common limitation of in situ measurements lies in appropriate selection of a representative site for complex urban components regardless of high cost and time needed for the work.

2.3.2 Remote Sensing Approach

Measuring all components of Eq. 2-1 can help predict UHI intensity, but gathering of these measurements is time consuming and impractical for vast urban environments. As a new research direction, urban thermal features can be extracted through remote sensing process and may be useful for obtaining UHI intensities. The influence from artificial source of heat has been commonly ignored in most UHI studies. Previous researches has concluded that the Q^* for typical

large urban cores is from 400 to 800 Wm^{-2} and Q_f has been found located generally between 20 and 200 Wm^{-2} in urban settings during hot months (Rigo and Parlow, 2007; Ichinose et al., 1999). Although Q_f can be relatively higher in winter due to heating of residential areas and transportation, its contribution to summer UHI is still controversial (Ichinose et al., 1999). With the popular of remote sensing satellite equipped thermal infrared remote sensors, it is possible and widely applied to study urban surface temperature as well as surface urban heat island (SUHI). The study can be more detail if the collected data with high temporal resolution and high spatial resolution at the same time are available. Regarding to the development tendency of thermal remote sensing in the research of SUHI effect, Voogt and Oke (2003) pointed out that: "Improvements in the spatial and spectral resolution of current and next-generation satellite-based sensors, in more detailed surface representations of urban surfaces and in the availability of low cost, high resolution portable thermal scanners are expected to allow progress in the application of urban thermal remote sensing to study the climate of urban areas."

2.3.2.1 Previous SUHI Studies

Many studies aim to study SUHI base on thermal infrared remote sensing. For the early years with only coarse resolution thermal images available, Rao (1972) used satellite thermal data (Improved TIROS Operational Satellite) of 7.4 km resolution to describe the thermal characteristics of cities along the coast. In the recent years with the enrichment of relative high spatial resolution data, Weng and Yang (2006) concluded that "more effort has been put to employ thermal infrared imagery from Landsat TM/ETM+, ASTER, and airborne Advanced Thermal and Land Applications Sensor (ATLAS), to study intra-urban temperature variations and to relate them to surface cover characteristics, which remains one hot issue and needs more solid research."

The UHI studies in selected cities of North America indicated that daytime thermal patterns were connected with land use which higher surface temperatures were observed in industrial areas with less vegetated coverage (Roth et al., 1989) by utilizing AVHRR thermal data. Gallo et al. (1993) revealed that the normalized difference vegetation index (NDVI) has inverse relationship with radiant surface temperature for the Seattle, United States. Weng et al. (2004) concluded that the scatterplot result of LST and NDVI showed a triangular shape and was affected by soil moisture conditions and the evaporation of the surface using case study in the city of Indianapolis, USA, where vegetation fraction was used as a new indicator instead of NDVI which presented best result around the resolution of 120 m. The study of a tropical city in Singapore observed that urban vegetation, surface geometry and building density may impact local air and surface temperature by analyzing Landsat TM data (Nichol, 1996). The UHI effect in Vancouver, Canada identified that the highest temperature area of downtown core is affected by existing thermal properties and the street geometry while the coolest intersection in the city was found to be attributed to vegetation (Ao and Ngo 2000). Principal component regression was conducted using SPOT images of Beijing, China and presented that LST was positively correlated with the population density (Xiao et al., 2008). A higher resolution (5m) airborne thermal infrared image data from ATLAS was utilized by Lo et al. (1997) which acknowledged previous study of strong negative correlation between NDVI and irradiance of urban surface. However, only limited articles studies the SUHI in the GTA, Canada. For example, Rinner and Hussain (2011) explored the relationship between land use and surface temperature by analyzing Landsat TM image acquired on September 3, 2008 for Toronto.

2.3.2.2 Selection of Remote Sensors

Thermal remote sensors (e.g. Landsat TM, ASTER) can be used to directly estimate land surface

temperature (LST) which are widely employed in previous studies mentioned above by converting digital number (DN) of each image pixel from satellite thermal data. Many methods have been tested to translate the value of calibrated thermal radiance to LST (Schott and Volchol, 1985; Goetz et al., 1995, Sobrino and Jimenez-Munoza, 2004). A question that must be taken into account in the estimation of surface temperatures of urban areas from captured imagery is to figure out what is actually being "seen" by the satellite sensors (Roth et al., 1989; Voogt and Oke, 2003).

For the early years, SUHI was normally studied using airborne infrared scanners or automobile surveys. A new form of instrumentation, satellite remote sensing became available after the launch of Television Infrared Observation Satellite (TIROS-1) in 1960, which provided the first set of atmospheric data from space. In 1964, the NIMBUS series of satellites which employed multispectral sensors for the measurement of atmospheric temperatures were launched as a follow on to TIROS-1. Because of their low spatial resolution, data from these early satellites is not suitable for study of features on the scale of urban environments. The first Geostationary Operational Environmental Satellite (GOES) by National Oceanic and Atmospheric Administration (NOAA) was launched in 1975. It provides increased spectral and spatial resolution compared to the NIMBUS series. However, the 4km ground pixel resolution in the thermal infrared band remains a limiting factor in UHI studies. Similarly, 1.1km spatial resolution AVHRR data were used to study UHI, but it was only suitable for large scale urban temperature mapping (Roth et al., 1989; Gallo et al., 1993). Since 1972, the Landsat series of satellites have been launched continually. The first Landsat satellite carried a multi-spectral sensor that could image the thermal infrared spectrum in 240m spatial resolution and enabled the study of urban features on a scale that was useful for UHI investigation. After the initial success of the Landsat

satellites, additional Landsat satellites were launched with improved spectral and spatial resolution. The Landsat Thematic Mapper (TM) and Enhanced Thematic Mapper Plus (ETM+) thermal sensors have a relatively fine ground pixel size (120m for TM and 60m for ETM+), capturing swaths of 185km with 16 day repeat cycles. Landsat 5 TM was launched in March 1, 1984 and provided more than 25 years of imagery before it stopped in November, 2011. Landsat 7 ETM+ has been running since April 15, 1999, however on May 31, 2003 the Scan Line Corrector (SLC) instrument failed. The SLC failure results in linear gaps of missing data within the acquired image after 2003. The Landsat 8 (LDCM) was launched on February 11, 2013 with two instruments, Operational Land Imager (OLI) and Thermal Infrared Sensor (TIRS). The Landsat 8 satellite images the entire Earth every 16 days in an 8-day offset from Landsat 7 with improved signal-to-noise (SNR) radiometric performance quantized over a 12-bit dynamic range. However, since the launch of Landsat 8 in 2013, thermal energy from outside the normal field of view (stray light) has affected the data collected in TIRS Bands 10 and 11. Advanced Spaceborne Thermal Emission and Reflection Radiometer (ASTER) on the Terra satellite was launched in December 1999. ASTER has three visible and near infrared (VNIR) bands and a near infrared backward-scanning band with the same resolution. ASTER also offers six short wave infrared (SWIR) and five thermal infrared (TIR) band, but ASTER is an on-demand instrument which prohibits continuous collection of image data. The Moderate Resolution Imaging Spectroradiometer (MODIS) which is equipped on the Terra satellite, provides information about the Earth's surface in 36 wavebands. The thermal band spatial resolution (1km) of MODIS is coarse although it has better spectral resolution. By examining the development of remote sensors, there is no spaceborne sensor can provide both high spatial resolution, spectral resolution and sufficient temporal resolution needed in SUHI studies so far. As a result, the selection of ideal satellite sensor needs to be considered regarding to different

study topics. From the aspect of spatial scale, previous studies of UHI, which use AVHRR or MODIS data are only suitable for large-area urban temperature mapping, not for accurate and meaningful evaluation (Weng, 2009). The Landsat TM (and later ETM+ and OLI/TIRS) and ASTER data have been extensively utilized to study UHI because its medium resolution TIR data can present different land uses or surface structures (Carnahan & Larson, 1990; Kim, 1992; Weng et al., 2004; Weng, 2006). Better spatial resolution is preferred when studying UHI at the micro-scale. From the aspect of spectral scale, multispectral TIR imageries are usually processed to recover LST by radiative transfer equation or split-window technique (Schmugge et al., 1998). Attentions also have been paid to recover LST from single-channel TIR data by single-channel algorithm or mono-window algorithm. However, multispectral TIR data are not frequently applied in UHI studies as most UHI studies are interested in relative LST measurements by mapping the spatial variations of UHI (Weng, 2009). Therefore, with the focuses on characterization of long term SUHI in the GTA, and limited satellites in orbit with TIR sensors of urban environmental imaging capacity, the most appropriate selection is Landsat series satellites and ASTER.

Chapter 3

Study Area and Data

3.1 Introduction

This thesis characterizes the SUHI of the City of Toronto and its surrounding areas obtained from satellite images which cover the most part of the Greater Toronto Area (GTA). The growing of the GTA is reflected by increasing of build-up areas and population. Toronto, as the core of the GTA, is a characteristic study subject located near 44˚N and along the western shore of Lake Ontario.

3.2 Study Area

The Greater Toronto Area (GTA), as shown in Figure 3.1, is one of the most quickly expanding metropolitan area in North America including five regions with a population of more than 6 million (Statistics Canada, 2011). Table 3.1 presents the population growth rates from 2006 to 2011 for different regions in the GTA. Figure 3.2 shows the growing of urban areas of the GTA since 1945.

Figure 3.1 Map of the GTA
(Source: Environment Canada, 2014)

Table 3.1 The population of the GTA.

Region	2006	2011	Change
City of Toronto	2,503,281	2,615,060	111,779 (4.5%)
Region of Peel	1,159,455	1,296,814	137,359 (11.8%)
Region of York	892,712	1,032,524	139,812 (15.7%)
Region of Halton	439,206	501,669	62,463 (14.2%)
Region of Durham	561,258	608,124	46,866 (8.4%)

(Sources: Statistics Canada 2011)

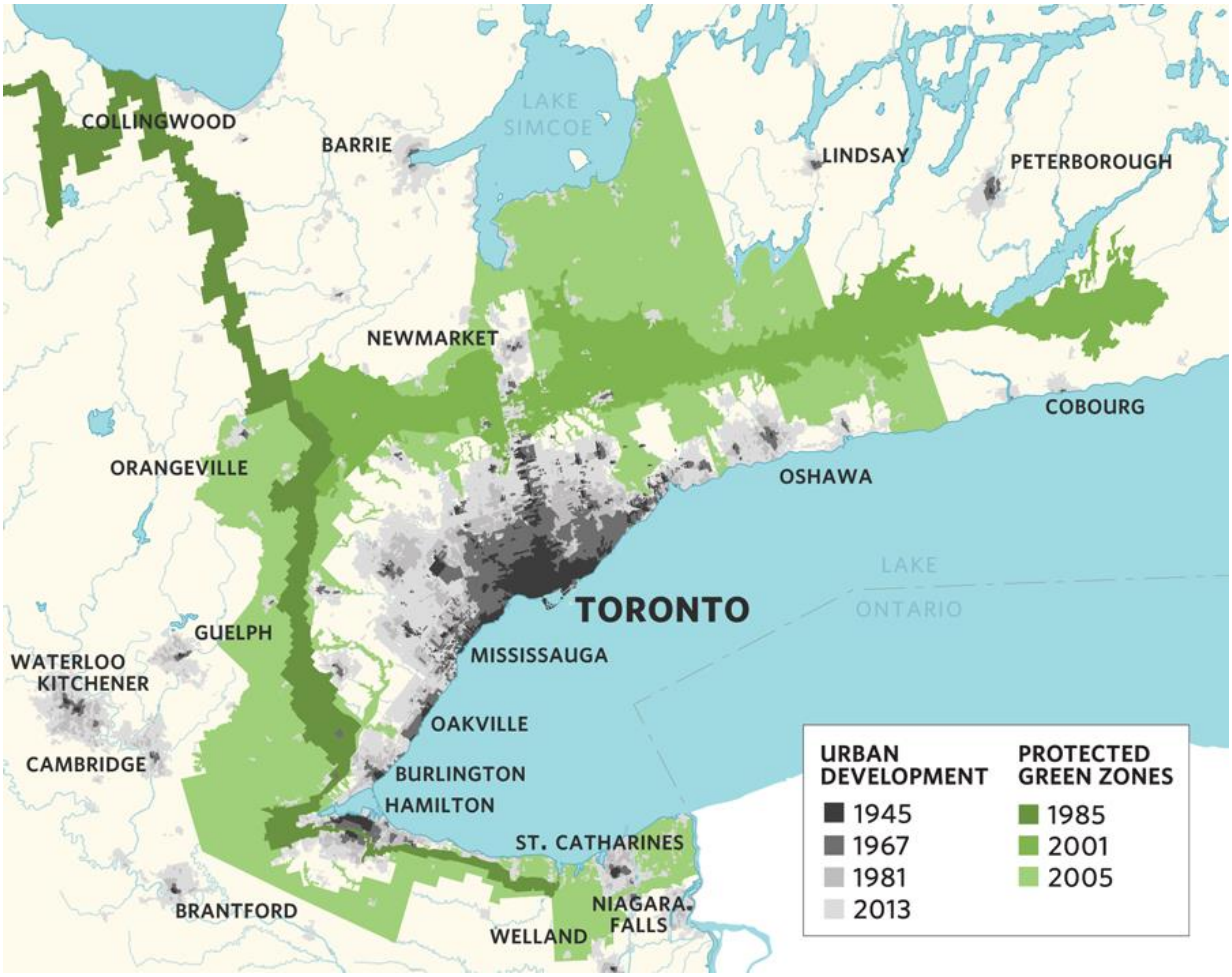

Figure 3.2 Change of the urban areas in the GTA
(Source: Greenbelt, 2014)

It is clearly seen from the Figure 3.2 that the main expansion of the city center started from 1945 to 1920. Another phenomenon of urbanization is the growth of population which is shown in

Figure 3.3 for the Toronto census metropolitan area (CMA) from 1931 to 2014. For recent decades, major increased population is international immigrants as the welcome policy for foreign labor force. In addition, people who come to Canada prefer settling in urban areas where provide convenient facilities and job opportunities.

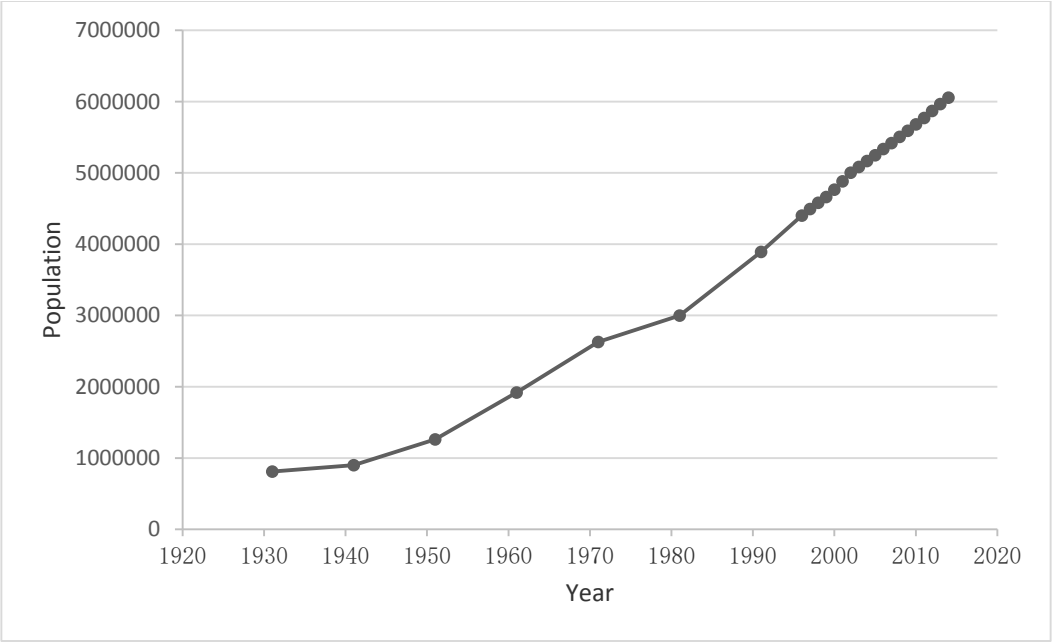

Figure 3.3 Population growth in Toronto CMA, 1931-2014
(Source: Statistics Canada, 2014)

3.3 Data

3.3.1 Satellite Images

Selected Landsat 5 TM images of path 18, row 29 and path 18, row 30 were acquired from website of the US Geological Survey (USGS) in GeoTIFF format between 1984 and 2013. The raster images for each scene include 7 tiff images for 7 bands separately. Each band monitors radiance within a specific section of the light spectrum. In this research, the thermal band (Band 6) images are key research contents with 120 m pixel resolution. The data package downloaded from the USGS comes with a metadata file including various parameters associated with the specific image.

Landsat 7 launched in 1999 carries the ETM+ sensor which provides the thermal band images with 60 m resolution. The failure of Scan Line Corrector (SLC) after May 31, 2003 leads to data gaps. Although the processing of filling data gaps has been widely studied, it still introduces errors when calculating pixel scale values. Landsat 8 is the latest operating (Feb, 2013) next-generation Landsat satellite. It is equipped with two spectral bands 100 m resolution thermal infrared sensor. The useful images are limited so far due to its short running time and stray light issues. ASTER images are available from 1999 to present with secondary higher resolution of 90 m. However, few images are eligible for study due to high cloud cover rate over the study areas. All used satellite images, which July and August no cloud images are preferred, are listed in Table 3.2 with associated same day meteorological conditions at 10:30 am recorded by the Pearson International Airport weather station. NA in Table 3.2 means no data available.

Table 3.2 Landsat and ASTER satellite images data summary and meteorological conditions

Sensor	Date	Resolution (m)	Air Temp (˚C)	Wind Speed (km/h)	Humidity (%)
Landsat 5 TM	July 31, 1984	120	26.1	21	29
Landsat 5 TM	July 8, 1987	120	28.4	9	37
Landsat 5 TM	July 24, 1987	120	30.7	22	40
Landsat 5 TM	August 14, 1989	120	25.7	7	31
Landsat 5 TM	August 30, 1989	120	23.1	41	26
Landsat 5 TM	August 6, 1992	120	23.0	7	25
Landsat 5 TM	August 22, 1992	120	22.8	4	27
Landsat 5 TM	August 9, 1993	120	23.5	4	28
Landsat 5 TM	August 25, 1993	120	27.7	10	35
Landsat 5 TM	July 11, 1994	120	21.6	7	25
Landsat 5 TM	July 14, 1995	120	31.0	18	43
Landsat 5 TM	July 30, 1995	120	25.2	2	29
Landsat 7 ETM+	July 17, 1999	60	31.7	28	41
Landsat 5 TM	July 25, 1999	120	29.3	24	34
Landsat 5 TM	July 11, 2000	120	23.8	25	26
Landsat 5 TM	July 27, 2000	120	24.9	11	31
Landsat 5 TM	August 12, 2000	120	22.6	19	26
Landsat 7 ETM+	August 20, 2000	60	16.3	22	NA

Landsat 5 TM	August 28, 2000	120	22.3	16	26
Landsat 7 ETM+	July 6, 2001	60	20.6	32	NA
Landsat 5 TM	July 14, 2001	120	22.9	32	26
Landsat 7 ETM+	July 22, 2001	60	27.9	11	36
Landsat 5 TM	July 30, 2001	120	22.9	15	26
Landsat 7 ETM+	August 10, 2002	60	26.5	12	29
Landsat 5 TM	August 18, 2002	120	25.0	25	28
Landsat 5 TM	July 25, 2005	120	31.9	29	37
Landsat 7 ETM+	August 5, 2006	60	24.5	13	29
Landsat 5 TM	August 13, 2006	120	21.2	13	26
Landsat 7 ETM+	August 21, 2006	60	23.8	12	25
Landsat 5 TM	July 1, 2008	120	23.5	15	25
Landsat 5 TM	July 17, 2008	120	25.1	9	31
Landsat 7 ETM+	July 25, 2008	60	25.4	16	29
Landsat 5 TM	August 18, 2008	120	26.5	28	33
Landsat 7 ETM+	August 26, 2008	60	20.1	8	NA
Landsat 5 TM	July 4, 2009	120	19.6	28	NA
Landsat 5 TM	July 20, 2009	120	22.0	10	25
Landsat 5 TM	August 5, 2009	120	20.7	23	25
Landsat 7 ETM+	August 13, 2009	60	25.3	8	32
Landsat 5 TM	August 21, 2009	120	24.9	23	31
Landsat 5 TM	July 7, 2010	120	31.3	8	42
Landsat 7 ETM+	July 15, 2010	60	27.2	15	36
Landsat 7 ETM+	July 31, 2010	60	22.9	8	26
ASTER	July 18, 2011	90	29.3	20	37
ASTER	August 12, 2011	90	25.1	7	28
Landsat 7 ETM+	August 19, 2011	60	27.4	11	30
Landsat 5 TM	August 27, 2011	120	24.2	2	29
Landsat 7 ETM+	August 8, 2013	60	24.0	6	29
Landsat 7 ETM+	August 24, 2013	60	21.9	14	26
Landsat 8 TIRS	July 8, 2014	100	24.3	17	32
Landsat 7 ETM+	August 11, 2014	60	25.0	16	31
Landsat 8 TIRS	August 19, 2014	100	20.8	12	25
Landsat 7 ETM+	August 27, 2014	60	22.0	11	26

3.3.2 Historical Climate Data

The weather stations are listed in Table 3.3 with detailed information about the stations. Figure 3.4 provides a map of weather station locations within study area by green dots. The temperature data are available from Environment Canada (EC) for each station. According to raw meteorological data, annual, seasonal and monthly mean temperature series can be calculated separately.

Table 3.3 Details for the selected stations

Station	Location	Elevation (m)	Type	Record
Downtown Toronto	43.67/-79.40	113	Urban	1840-2014
Pearson Int'l. Airport	43.68/-79.63	173	Urban	1938-2014
Richmond Hill	43.88/-79.45	240	Suburban	1960-2014
Oshawa	43.87/-78.83	84	Suburban	1969-2014
Beatrice (outside GTA)	45.15/-79.40	297	Rural	1876-2014

Figure 3.4 Weather station locations

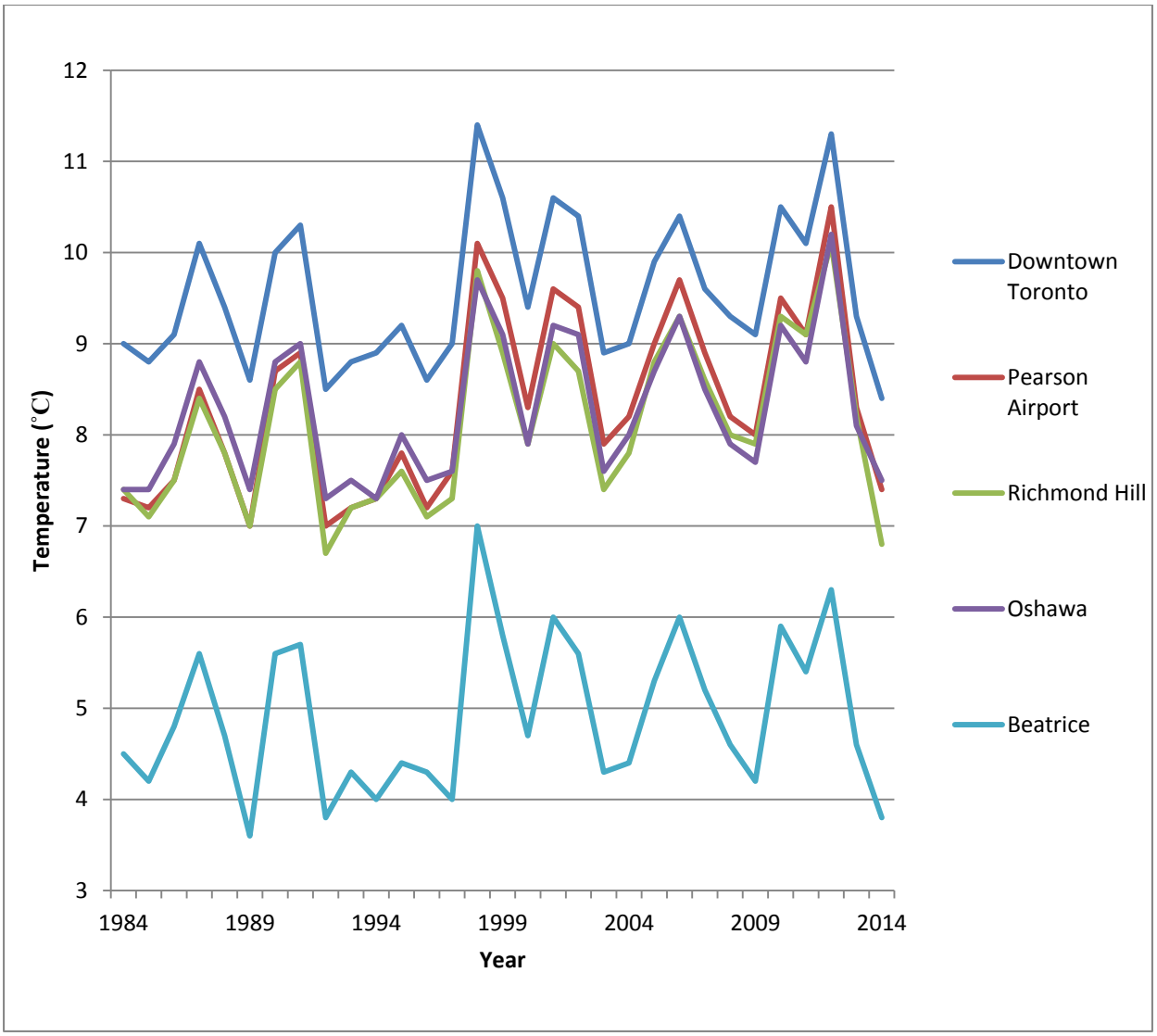

Figure 3.5 Annual mean temperature trends for each location

Figure 3.5 shows the annual mean temperature trends for five study locations. The graphs present the unified trends for both five locations from 1984 to 2014 but with regional temperature differences. In this case, the temperature of downtown Toronto is generally the highest compared with nearby locations. Detailed analysis and evaluation will be presented in Chapter 5 regarding to UHI effect.

3.3.3 Supplementary Data

Extra data (Table 3.4) can be helpful when analyzing and evaluating the original data. For instance, in order to clip out the GTA, the study area in this thesis, a shapefile which covers the boundary of the study area is obtained from the University of Waterloo Geospatial Centre. The boundary map is produced and projected in Geographic Coordinate Systems (GCS_North_American_1983) using North American Datum of 1983 (NAD83). Additionally, 1:50,000 geo-base road networks of GTA is used for geometric correction of images. The land use shapefile and population data are incorporated to better understand SUHI at specific locations precisely.

Table 3.4 Supplementary data

Data	Year	Source
GTA Boundary	2011	Statistics Canada
Population	2011 & 2001	Statistics Canada
Road Network	2014 & 2006	Ontario Ministry of Transportation
Land Use	2014 & 2008	Ontario Ministry of Natural Resources

Chapter 4

Methodology

This chapter illustrates the processes to characterize UHI and SUHI, to describe temperature trend and to map the SUHI patterns. The major methods (trend analysis and thermal images mapping) will be explained sequentially in the following sections of this chapter. Figure 4.1 shows the whole procedure as a flowchart. Left box in Figure 4.1 shows the thermal images processing procedure with input data of raw satellite images and supplementary data, such as population, land use and road network. The output, LST maps, will be interpreted with those supplementary data in order to characterize SUHI by thematic maps. LST is also compared with historical temperature to see if significant correlation exists. For the right side of Figure 4.1, which is outlined by orange dash line, is the procedure for trend analysis. The input historical meteorological data will be tested by trend analysis, and used to describe the UHI intensity afterwards.

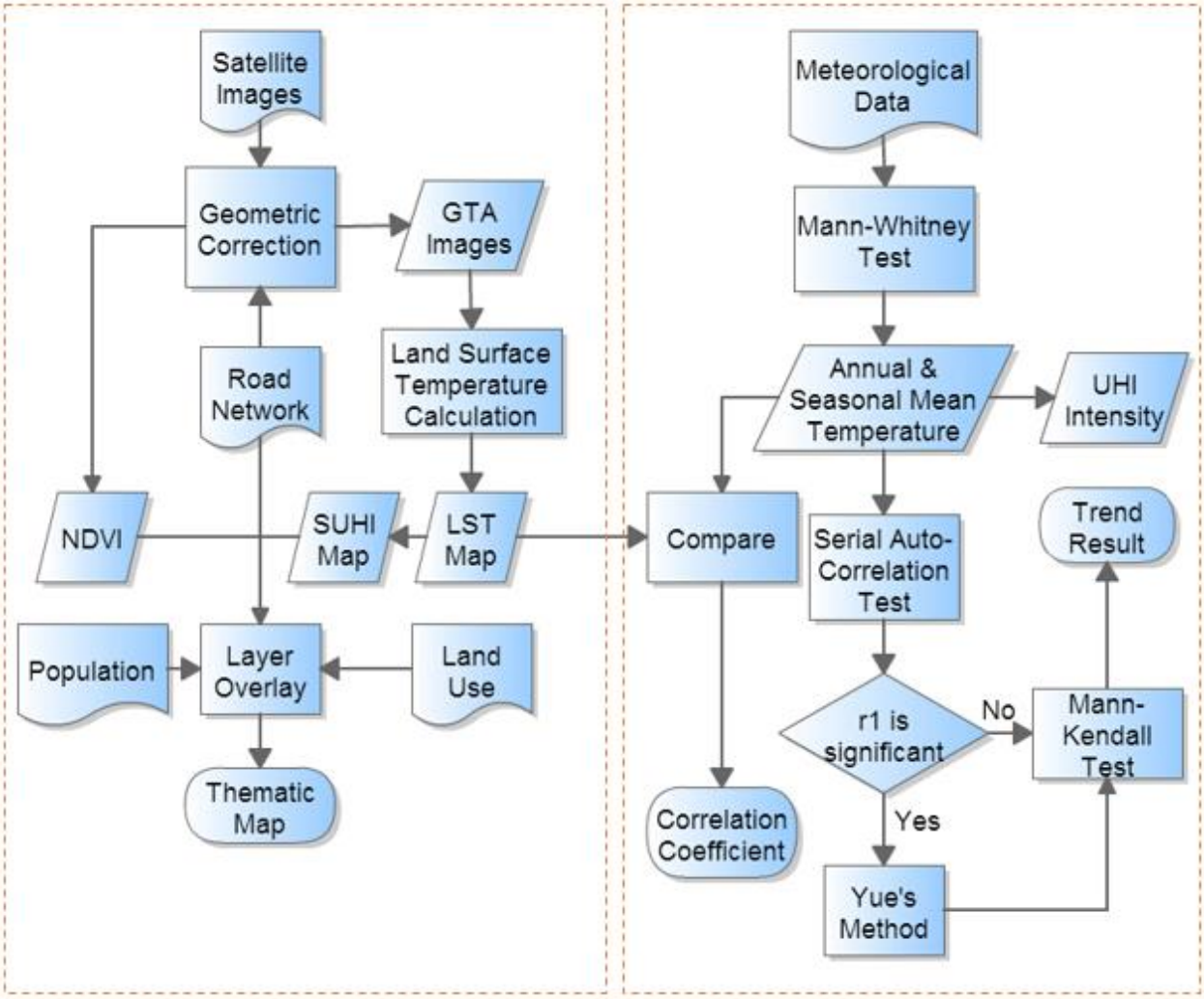

Figure 4.1 Flowchart of the methodology

4.1 Data Preprocessing

4.1.1 Meteorological Data Preprocessing

The time series used in the trend analysis are commonly tested for homogeneity by using the Mann-Whitney (MW) test (also known as Mann-Whitney-Wilcoxon test). The superiority of MW test compared to other tests like t-test is the nonobligatory requirement of normal distribution datasets which makes it applicative for temperature measurements (von Storch & Zwiers, 2003). In meteorology, temperature datasets are usually recorded continuously for years. During the study period, certain stations may encounter problems such as missing data, change of measurement

locations and update of instruments, therefore, the MW test insure the robustness and effectiveness of the data. The MW test, which is a non-parametric style test, identifies sample differences by first ranking all the combined sample contents with sequence regarding to sample means and medians. The sum of ranks for each tested sample should present similar result to each other when same data distribution is observed in both samples (Yue & Wang, 2002). The result of Mann-Whitney Test is listed in Table 4.1. Only two sites (Downtown Toronto and Beatrice) need to be tested as the other three are already adjusted and homogenized data obtained from Environment Canada (Vincent et al., 2012). According to results in Table 4.1, two stations' p values are both larger than 0.05 and past the homogeneity test which insure the robustness and effectiveness of the data.

Table 4.1 Mann-Whitney test for two weather stations

Station name	Median of Group 1	Median of Group 2	p-value (α=0.05)
Downtown Toronto	9.0	9.8	0.0501
Beatrice	4.4	5.3	0.1004

4.1.2 Satellite Image Preprocessing

Two images from the same date are merged to cover the potential extent of study area in ENVI 5.1 (Figure 4.2). In order to have consistent presentation of images, all images from different satellite sensors are resampled to 30 m. Then study area is clipped out from mosaic images by taking a shapefile representing the GTA boundary as the base map (Figure 4.3). For comparing derived surface temperature with historical air temperature or other dataset at minimum positional error, geometric correction is applied to images based on a reliable source which is 1:50,000 geo-base GTA road networks. 25 evenly distributed ground control points (Figure 4.4) are selected for each scene to generate georeferenced thermal band images.

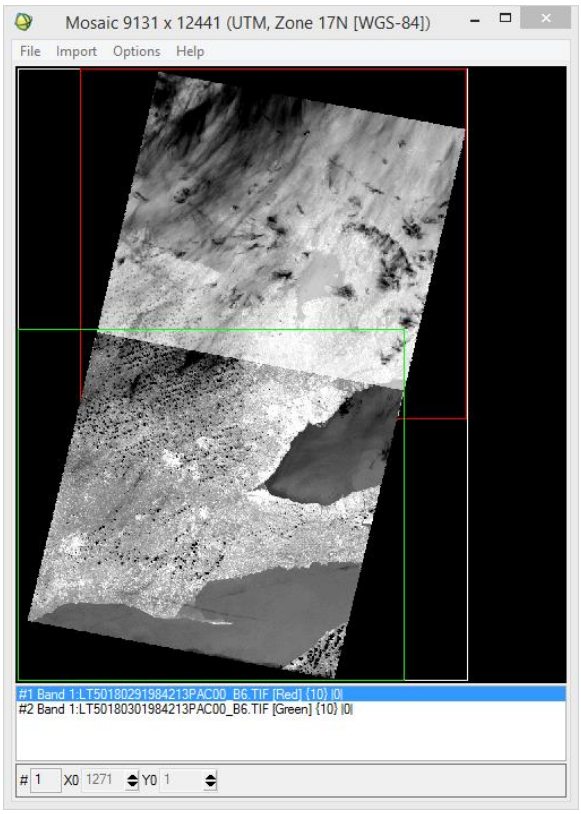

Figure 4.2 Mosaicking of two images

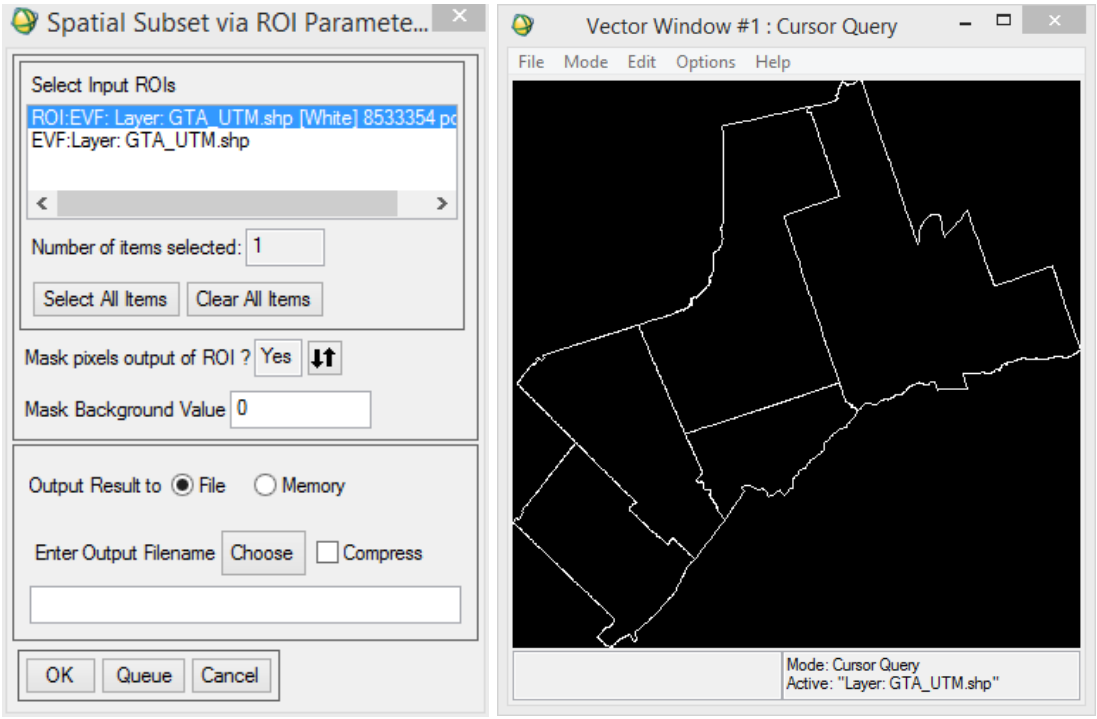

Figure 4.3 Clipping of study area

Figure 4.4 Distribution of ground control points

An optional preprocessing step is to apply atmospheric correction to satellite images. If absolute temperature needs to be studied precisely, atmospheric correction is an essential step before generating LST map. For this study, long term trends and geographical distribution of SUHI are more focused. Although NASA provides an online tool called Atmospheric Correction Parameter Calculator (ACPC) in 2003 (http://atmcorr.gsfc.nasa.gov) to calculate atmospheric transmission, downwelling and upwelling radiance easily, data are only available starting from 2000.

4.2 Data Analysis

4.2.1 Trend Analysis

4.2.1.1 Testing for serial auto-correlation

The serial auto-correlation could be existed due to inner relationship presented within time series observations regarding to adjacent data. The prerequisite for employing of MK trend test is that all the observed values in a time series are independent, but the serial auto-correlation will increase the sample differentiation. Therefore, the MK test may tend to overestimate or underestimate significant trend in the time series (Helsel & Hirsch, 2002) if serial auto-correlation exists in the dataset. In order to reduce the effect of serial auto-correlation, von Storch (1995) suggested to pretreat the time series before processing the MK test, which means the first step before applying Mann-Kendall (MK) trend analysis is to test for serial auto-correlation of each time series. The method used to remove the time series lag-1 correlation coefficient is autoregressive and integrated moving average (ARIMA) model, which is a dependent time series that is modeled as a linear combination of its own past values and past values of an error series. Nonetheless, it is noticeable that the ARIMA method could influence the final result of the trend by removing some trend details and mitigating the serial autocorrelation in the data at the same time (Zhang et al., 2000, Yue et al., 2002). The procedure for the data pretreatment is listed as following: 1) calculate the serial auto-correlation coefficient (r_1), 2) check the significance of r_1 at the 0.05 level, MK test is applied to original dataset if it is not significant, 3) if the computed r_1 is significant, the Yue's (2002) method is used to eliminate r_1 before the test. The serial correlation is tested using Minitab 17 and results are listed in Table 4.2 for all the stations used in this study.

Table 4.2 Autocorrelation coefficients for the period of 1984 – 2014 (*indicates that data is serially correlated at 0.05 level)

Station	Lag-1	Lag-2	Lag-3
Downtown Toronto	0.221	-0.265	0.013
Pearson Int'l Airport	0.380*	-0.016	0.153
Richmond Hill	0.313	-0.151	0.078
Oshawa	0.198	-0.225	-0.003
Beatrice	0.135	-0.290	0.012

Data from the Pearson International Airport shows autocorrelation at 0.05 level for annual mean temperature according to the test result in Table 4.2. The other four stations do not present autocorrelation for the data serial.

4.2.1.2 Mann-Kendall (MK) Test

The MK test inspects the variation tendency of observations over the time in the data. When x-axis indicates time i.e. year in this study, the MK test is also known as Kendall's tau. For this study, the null hypothesis is that there is no trend exists in the time series, in other words, the alternative hypothesis gives that a variation trend appears within the time series. In the test, significant level of 0.05 are set to test the statistical significance for a two-sided probability. The MK test only predicts the series trend but do not provide a quantitative estimator of the trend. The traditional slope estimate like least-squares method is not robust enough in a non-parametric situation. For this purpose, the Theil-Sen approach (TSA) is applied to estimate the trend quantitatively because this method can decrease effects from abnormal or extreme temperature records in the time series (Sen, 1968).

4.2.2 Land Surface Temperature Estimation

Satellite images store the thermal band temperature information as a digital number (DN). DN is the sensor values usually ranged between 0 and 255 depends on the satellite. As a result, the first step for LST conversion is to convert imagery digital numbers to Top of Atmosphere radiance values (ToA_r) according to spectral radiance scaling method. The formula is as follows:

$$ToA_r = \frac{R_{Max} - R_{Min}}{Q_{Max} - Q_{Min}} * (DN - Q_{Min}) + R_{Min} \quad (4\text{-}1)$$

where R_{Max} and R_{Min} are the reference radiance range for each band correspondingly from metadata file. Q_{Max} and Q_{Min} are equal to the range of digital number to store cell value. DN is the known digital number per pixel and ToA_r is the calculated Top of Atmosphere radiance value per cell. For Landsat 5 TM, data are stored by 8-bit pixel values which means the corresponding Q_{Max} is 255 (Q_{Max} = 65,535 for 16-bit Landsat 8 data). Eq. 4-1 can be further simplified as a gain and bias method in Eq.4-2:

$$ToA_r = Gain * DN + Bias \quad (4\text{-}2)$$

where:

Gain = $\frac{R_{Max} - R_{Min}}{Q_{Max}}$

Bias = R_{Min}

Next step is to calculate LST using an inverse Planck function, shown in Eq. 4-3, where K_1 and K_2 are calibration constants. Table 4.3 lists the calibration constants for Landsat satellites and ASTER. R is spectral radiance derived from previous step and LST is calculated surface temperature in Kelvin.

$$LST = \frac{K_2}{ln\left(\frac{K_1}{R} + 1\right)} \quad (4\text{-}3)$$

Table 4.3 Thermal band calibration constants

Constant	K_1	K_2
Units	$W/(m^2.sr.\mu m)$	Kelvin
Landsat TM	607.76	1260.56
Landsat ETM+	666.09	1282.71
Landsat TIRS	774.89	1321.08
ASTER	865.65	1349.82

This two-step method is an image-based method, other popular algorithms with general higher accuracy including the Mono-Window Algorithm (Qin et al., 2001) and Single-Channel Method (Jiménez-Muñoz et al., 2009). Nevertheless, this two methods require the consideration of detailed atmospheric parameter related data such as atmospheric transmittance, land surface emissivity and near-surface humidity. These data are incomplete for some locations especially in the early stage of meteorological record. Another method called Split-Window Algorithm (Rozenstein et al., 2014) using two thermal band to calculate LST which only applies to Landsat 8. Similar to Split-Window Algorithm, Multiple-Channel Algorithm (Mao et al., 2006) is developed to retrieve LST from ASTER and MODIS data. The limitation of achievable quality images from ASTER and MODIS for the GTA area makes it inapplicable to all scenes in this study.

4.3 Validation

To validate the relative accuracy of LST results, LST maps are compared to weather stations' air temperature records from where different urban cover category is corresponding. It is barely possible to have in situ equipment measuring the whole 120 m by 120 m areas in order to satisfy the image pixel scale. However, previous studies have done similar tests to assess the accuracy of satellite image based LST and indicated that a rigorous validation is not necessary (Schneider & Mauser, 1996).

Chapter 5

Results and Discussions

In this chapter, the historical air temperature (AT) data from selected weather stations will be explored at first by discovering the underlying UHI trends and features. With the basic understanding of UHI trends in the GTA as reference, characterization of SUHI is followed by connecting satellite derived LST maps with vegetation, land use, population and road network. Tables, charts and thematic maps will be used to demonstrate the findings in each section.

5.1 Historical Trends Analysis Regarding to UHI

Simple linear regressions of annual mean temperature for five weather stations are obtained to give a rough idea about the variation trends during the time period 1984 – 2014. The plots of linear regression results and coefficient of R^2 are summarized in Figures 5.1 – 5.5 and Table 5.1.

Figure 5.1 Annual mean temperature variations in downtown Toronto from 1984 to 2014

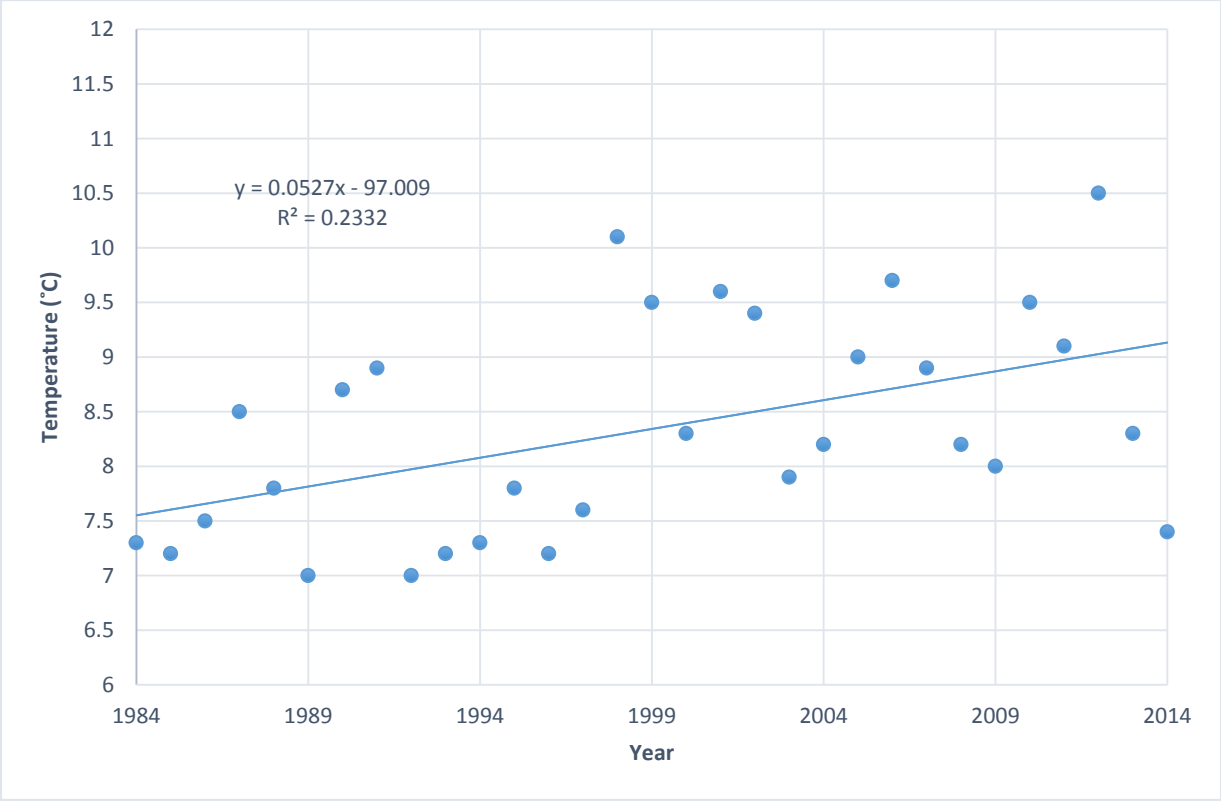

Figure 5.2 Annual mean temperature variations in the Pearson International Airport from 1984 to 2014

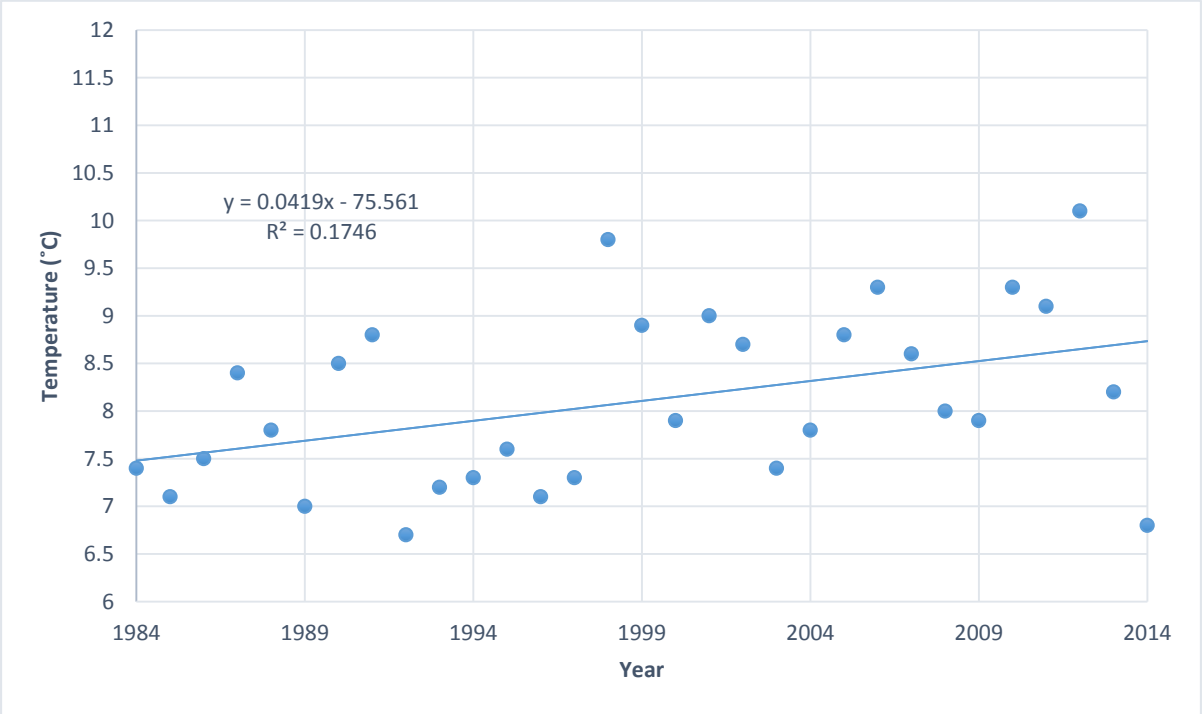

Figure 5.3 Annual mean temperature variations in Richmond Hill of the GTA from 1984 to 2014

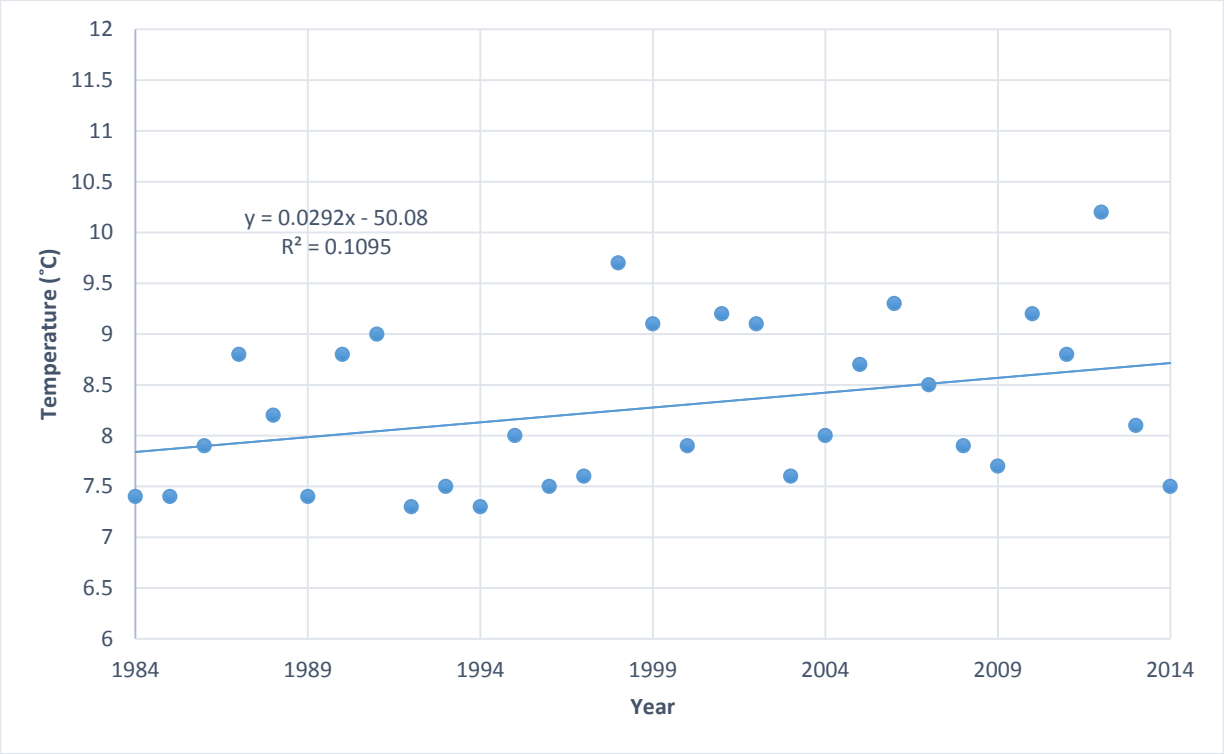

Figure 5.4 Annual mean temperature variations in Oshawa of the GTA from 1984 to 2014

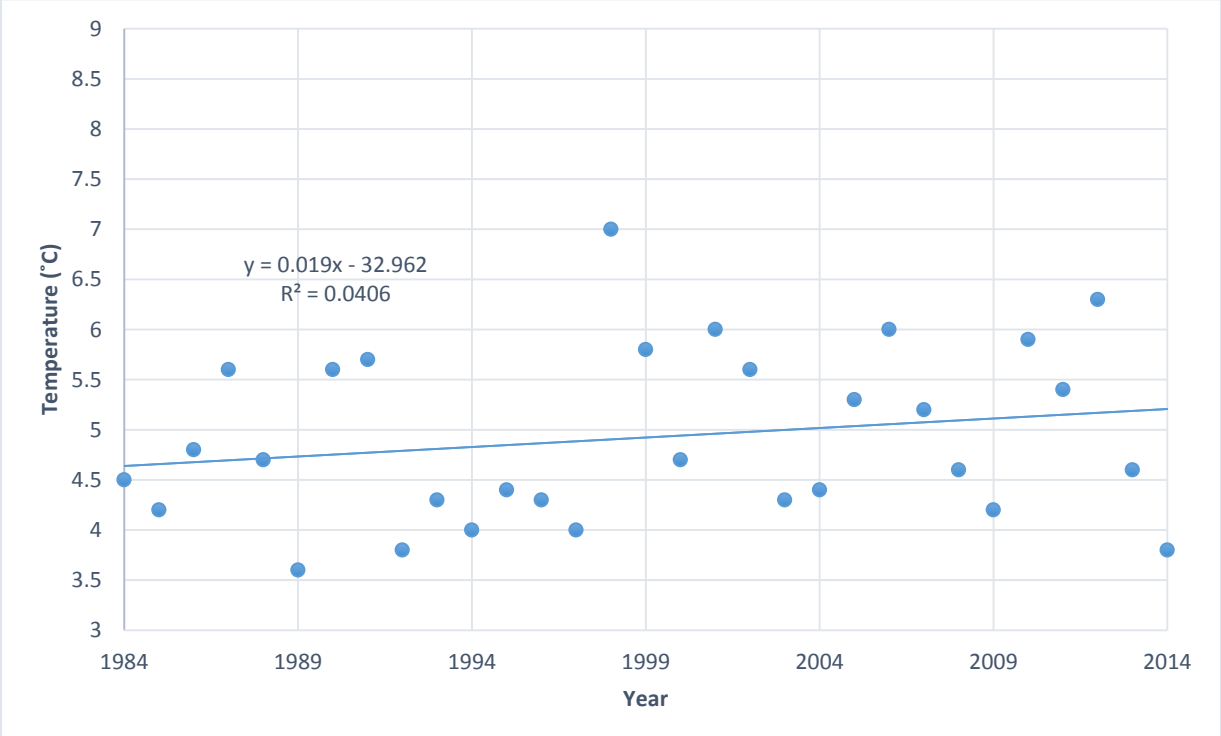

Figure 5.5 Annual mean temperature variations in Beatrice from 1984 to 2014

According to Figures 5.1 to 5.5, all five locations present weak but positive temperature trends from 1984 to 2014 with R^2 ranges from 0.041 to 0.233 in Table 5.1. The low R^2 value could be due to short time periods of available data. Additionally, the extreme values will be more influencing in small dataset. The complex driven factors of temperature will also weak the stability of trend. However, the significance of positive trends is corresponding to the R^2 values in Table 5.1, where the highest two R^2 values are significant at 0.05 level. The urban area (downtown Toronto) shows steady increasing rate of 0.023 which is not the highest case in this study. The possible reason for the mitigatory trend is the development of downtown Toronto has reached saturation. The highest significant increasing rate emerges at location of the Pearson International Airport. The booming of the Pearson International Airport area and surrounding areas by increasing industrial land contributes to the rapidly temperature change.

Table 5.1 Results of simple linear regression analysis

Station	Coefficient of determination	Trend	R^2 (* significant at 0.05 level)
Downtown Toronto	0.023	+	0.066
Pearson Int'l Airport	0.053	+	0.233*
Richmond Hill	0.042	+	0.175*
Oshawa	0.029	+	0.110
Beatrice	0.019	+	0.041

The MK trend test is applied after pretreatment of data and is used to predict the series trend. The test result is indicated in Table 5.2. A clear trend is observed from table below by examining statistical significance at 0.05 level. Annual mean temperature are significant at 0.05 level for the Pearson International Airport, Richmond Hill and Oshawa stations which indicate a solid increasing temperature trend.

Table 5.2 Mann-Kendall trend test and statistical significance of the trend

Stations	Annual mean temperature (* significant at 0.05 level)	
	Z	p-value
Downtown Toronto	1.481	0.069
Pearson Int'l Airport	2.703	0.003*
Richmond Hill	2.515	0.006*
Oshawa	1.972	0.024*
Beatrice	1.056	0.146

In order to get a quantitative estimator of the trend, Kendall's tau and slope were tested. Table 5.3 shows the result of both classic and Yue and Wang (2002) Kendall's tau and slope. Two methods give the same Kendall's tau values for each station. However, the significant level for trend slope is different for some stations. Kendall's tau and slope show the same result as Mann-Kendall trend test that highly expanded areas outside the city centre are experiencing the aggravated UHI.

Table 5.3 Classic & Yue and Wang Kendall's tau and slope (α=0.05)

Stations	Classic method		Yue and Wang's method	
	Kendall's tau	slope	Kendall's tau	slope
Downtown Toronto	0.230	0.025	0.230	0.025
Pearson Int'l Airport	0.346	0.056*	0.346	0.056*
Richmond Hill	0.320	0.044*	0.320	0.044*
Oshawa	0.265	0.024*	0.265	0.024
Beatrice	0.187	0.018	0.187	0.018

Figure 5.6 shows the annual temperature and UHI intensity from 1984 to 2014 by comparing urban area (downtown Toronto) with rural area (Beatrice). The temperature difference between urban and rural area of each year is described by grey bar (i.e. UHI intensity). The strongest UHI intensity since 1984 appears in the recent five years which is 5.7˚C in 2013. The trends of UHI intensity is not increased year by year but has a general upward tendency.

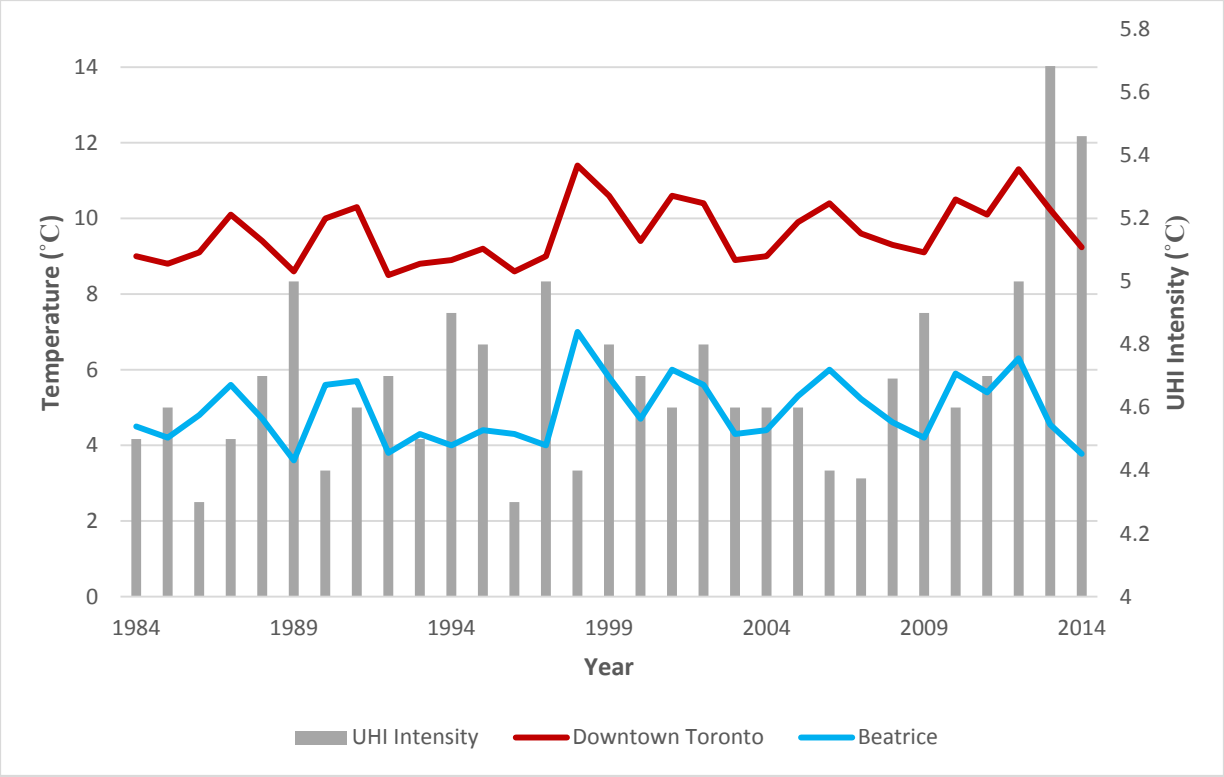

Figure 5.6 Annual UHI intensity (urban vs. rural) from 1984 to 2014

Figure 5.7 shows the seasonal UHI intensity from 1984 to 2014 by comparing urban area (downtown Toronto) with rural area (Beatrice). From the graph, the strongest UHI intensity mostly appears in the winter since 1984 with highest of 7.1˚C in 2003. It is not surprising that the UHI intensity in winter is generally stronger than traditional hot days in summer. The high latitude of the GTA increasing the need of heat supply during the winter which contributes the unique UHI phenomenon in the GTA. However, the UHI intensity is quantified by relative temperature difference between urban and rural area. Even under high UHI situation during the winters, the weather is still cold with temperatures normally below zero. When considering UHI intensity of spring, summer, fall and winter separately, the seasonal UHI intensity does not present significant increasing trend like annual UHI intensity for the past 30 years in the GTA.

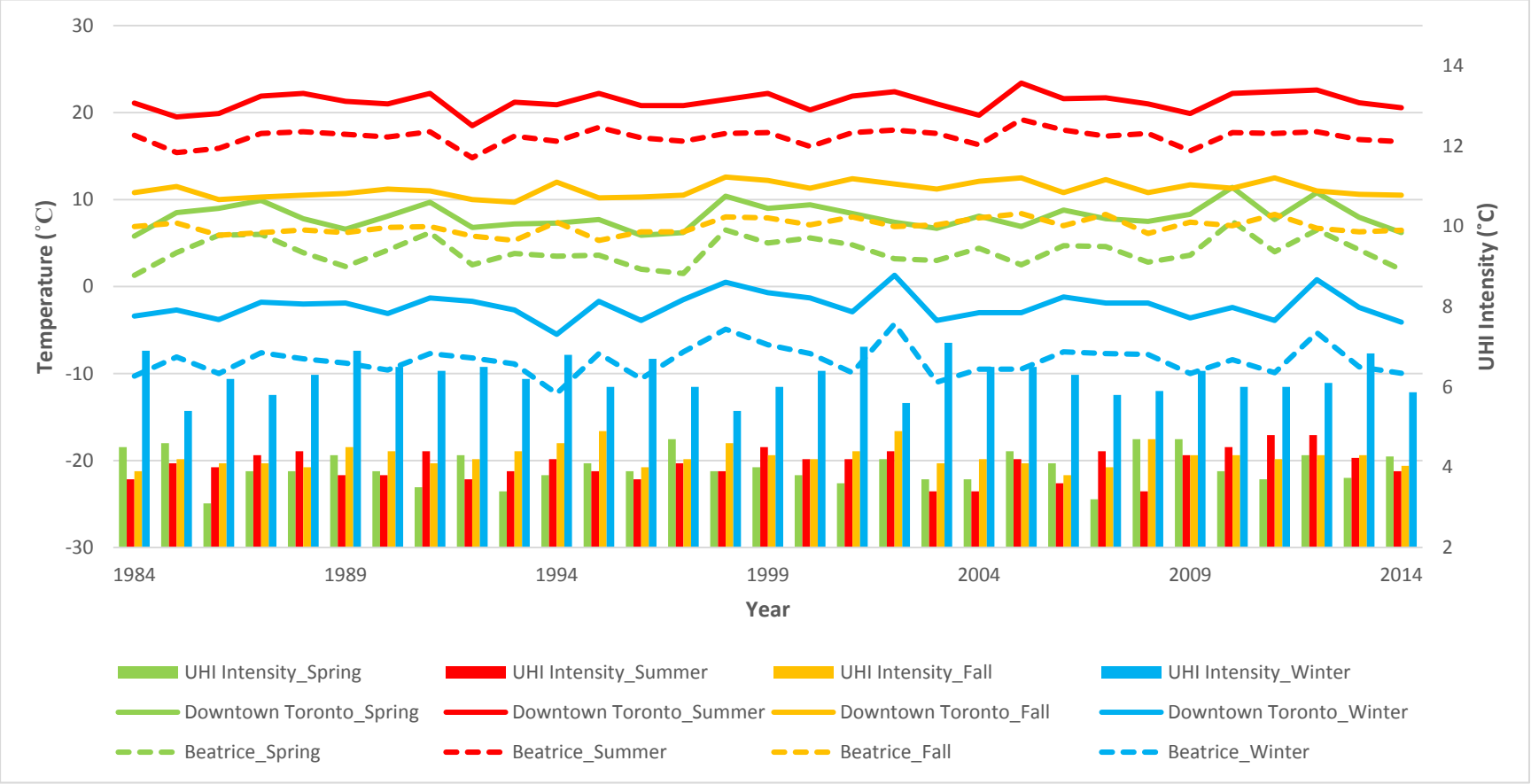

Figure 5.7 Seasonal UHI intensity (urban vs. rural) from 1984 to 2014

5.2 Remotely Sensed SUHI

Historical AT data reveals the characteristic of UHI and temperature trend from the aspect of temporal context in last section. The following sections will explore the SUHI characteristic spatially by mapping the features base on urban characteristics.

5.2.1 Satellite Derived LST

Figure 5.8 shows an example of LST map of the GTA in July 11, 1994. The figure demonstrate the surface temperature classified by standard deviation where blue means relatively low temperature areas and red means high temperature spots within the GTA boundary. The more evident of the colour difference, the more serious the SUHI presents. From Figure 5.8, most of the red part which has higher temperature is distributed in the urban area. All calculated pixel values which indicate the temperature of selected weather stations are compared with same day weather stations' records at the same time and the results are shown in Table 5.4. As satellite images are captured around 10:30 am of local time, paired air temperature is the average of records at 10:00 am and 11:00 am. From 1984 to 2014, in order to minimize the bias of calculated LST and increase the comparability of two dataset, the temperature is compared only when more than two scenes are available within the same month. Station in Beatrice is outside the GTA boundary as a rural reference and Station of Richmond Hill and Oshawa do not have hourly data. Therefore these stations are not included in Table 5.4.

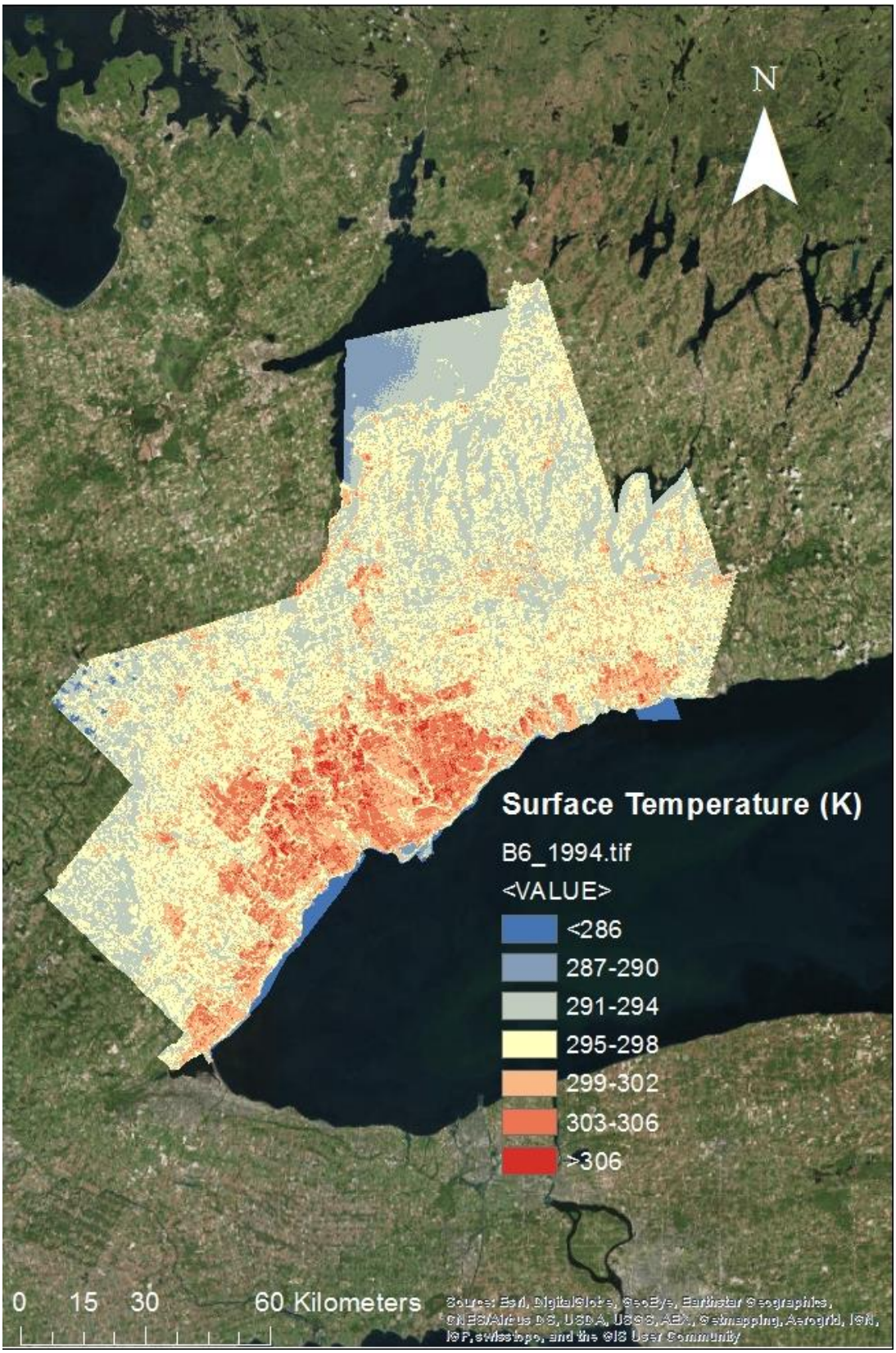

Figure 5.8 LST map of the GTA in July 11, 1994

Table 5.4 Comparison of weather stations' data with calculated LST (˚C) of pixel locations

Date	Downtown Toronto	LST	Pearson Int'l Airport	LST
July 8, 1987	26.7	29.5	28.4	33.7
July 24, 1987	25.3	32.0	30.7	33.7
August 14, 1989	21.1	26.0	25.7	24.7
August 30, 1989	23.2	25.8	23.1	29.1
August 6, 1992	19.3	20.3	23.0	23.3
August 22, 1992	19.2	21.2	22.8	25.4
August 9, 1993	21.0	27.4	23.5	29.5
August 25, 1993	25.4	27.5	27.7	28.5
July 14, 1995	24.8	31.1	31.0	38.9
July 30, 1995	24.9	26.8	25.2	30.1
July 17, 1999	23.4	28.4	31.7	32.7
July 25, 1999	30.3	27.3	29.3	28.5
July 11, 2000	24.3	28.0	23.8	22.9
July 27, 2000	22.4	28.1	24.9	30.8
August 12, 2000	21.1	25.7	22.6	26.9
August 20, 2000	16.6	22.0	16.3	20.6
August 28, 2000	20.3	21.5	22.3	25.3
July 6, 2001	20.8	20.1	20.6	27.1
July 14, 2001	22.1	26.4	22.9	25.3
July 22, 2001	23.1	27.7	27.9	33.4
July 30, 2001	21.8	25.1	22.9	26.5
August 10, 2002	22.9	27.8	26.5	30.2
August 18, 2002	24.6	23.8	25.0	25.8
August 5, 2006	24.0	28.7	24.5	31.3
August 13, 2006	22.3	25.9	21.2	23.9
August 21, 2006	23.4	30.6	23.8	27.1
July 1, 2008	21.8	29.9	23.5	25.4
July 17, 2008	25.2	26.2	25.1	26.3
July 25, 2008	24.4	21.7	25.4	25.4
August 18, 2008	25.6	29.3	26.5	31.0
August 26, 2008	19.9	23.8	20.1	22.2
July 4, 2009	19.8	26.3	19.6	27.1
July 20, 2009	20.7	25.6	22.0	29.5
August 5, 2009	20.7	25.6	20.7	29.4
August 13, 2009	26.1	33.9	25.3	32.8
August 21, 2009	24.2	31.1	24.9	32.3
July 7, 2010	29.5	35.2	31.3	40.7
July 15, 2010	26.9	31.9	27.2	33.5
July 31, 2010	22.8	24.8	22.9	26.9
August 12, 2011	26.0	27.4	25.1	24.8
August 19, 2011	27.7	36.6	27.4	35.8
August 27, 2011	25.0	29.7	24.2	27.3

August 8, 2013	25.3	29.4	24.0	31.1
August 24, 2013	22.5	26.5	21.9	27.4
August 11, 2014	25.1	29.9	25.0	29.7
August 19, 2014	19.5	26.1	20.8	22.9
August 27, 2014	22.2	26.4	22.0	29.6

When examining Table 5.4, there is difference between the weather stations' data and calculated LST value. Studies have been done to explore the relationships between derived LST and air temperature. However, no reliable approach is universally adoptable regarding to very complex urban environment diversity (Voogt & Oke, 2003). Klok et al. (2012) found a strong correlation (R^2 = 0.81) between LST and air temperature by comparing four Landsat images from 2005 to 2007 with air temperature measured by weather stations at Rotterdam in the Netherlands. Similar analysis was done (R^2 = 0.52) in Montreal by using 12 Landsat images from 1984 to 2011 (Martin et al., 2015). In this study, 47 pairs of LST and weather stations' data are also plotted from 1984 to 2014 in Figure 5.9 which shows a strong relationship between LST and air temperature of the weather station in downtown Toronto, with R^2 = 0.48 and Pearson's correlation coefficient (P) of 0.696 (significant at 0.001 level). Result shown in Figure 5.10 for the weather station of the Pearson International Airport also concurs with previous work of Klok et al. (2012) and Martin et al. (2015) by R^2 = 0.55 and Pearson's correlation coefficient of 0.738 (significant at 0.001 level). Based on Figure 5.9 and Figure 5.10, satellite derived LST has the potential to be indicator of variations in air temperature due to high relevancy. This conclusion is reasonable because it is based on the principle that surface and air temperatures are convertible through diabatic fluxes by the form of sensible heat, radiative fluxes and latent heat.

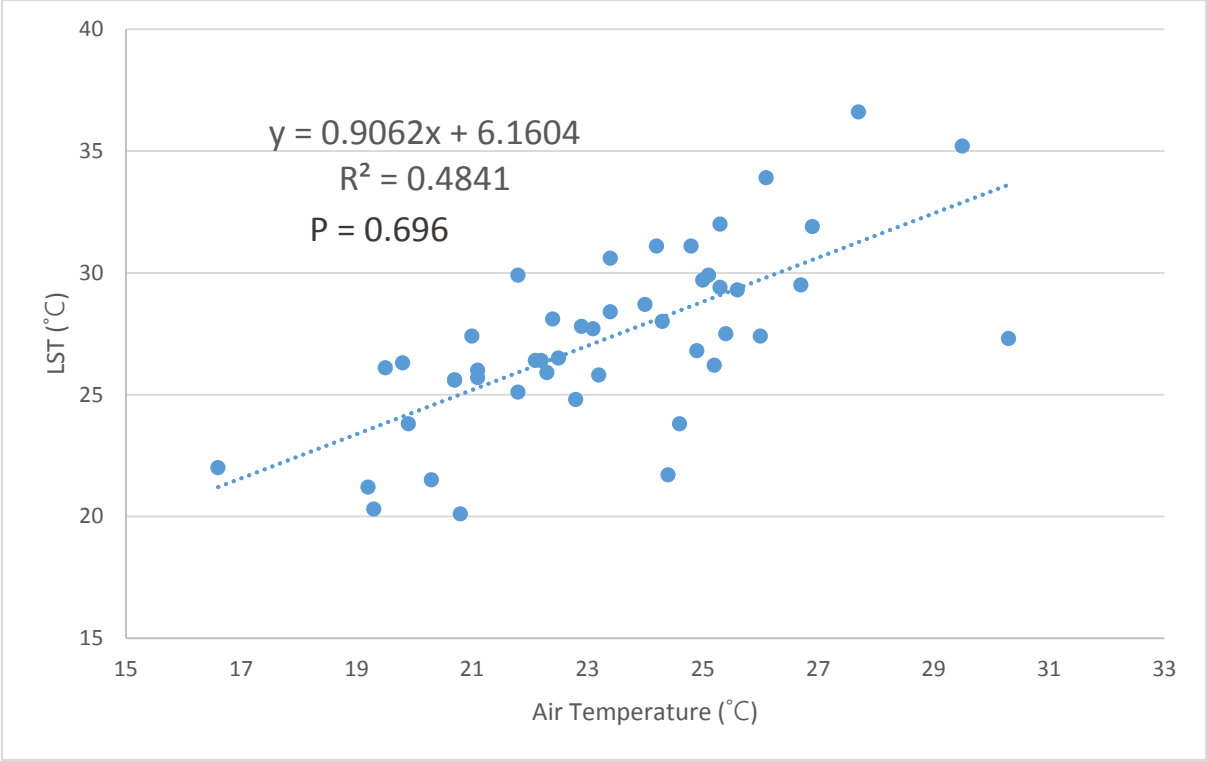

Figure 5.9 LST of pixel location vs. air temperature at weather station of downtown Toronto

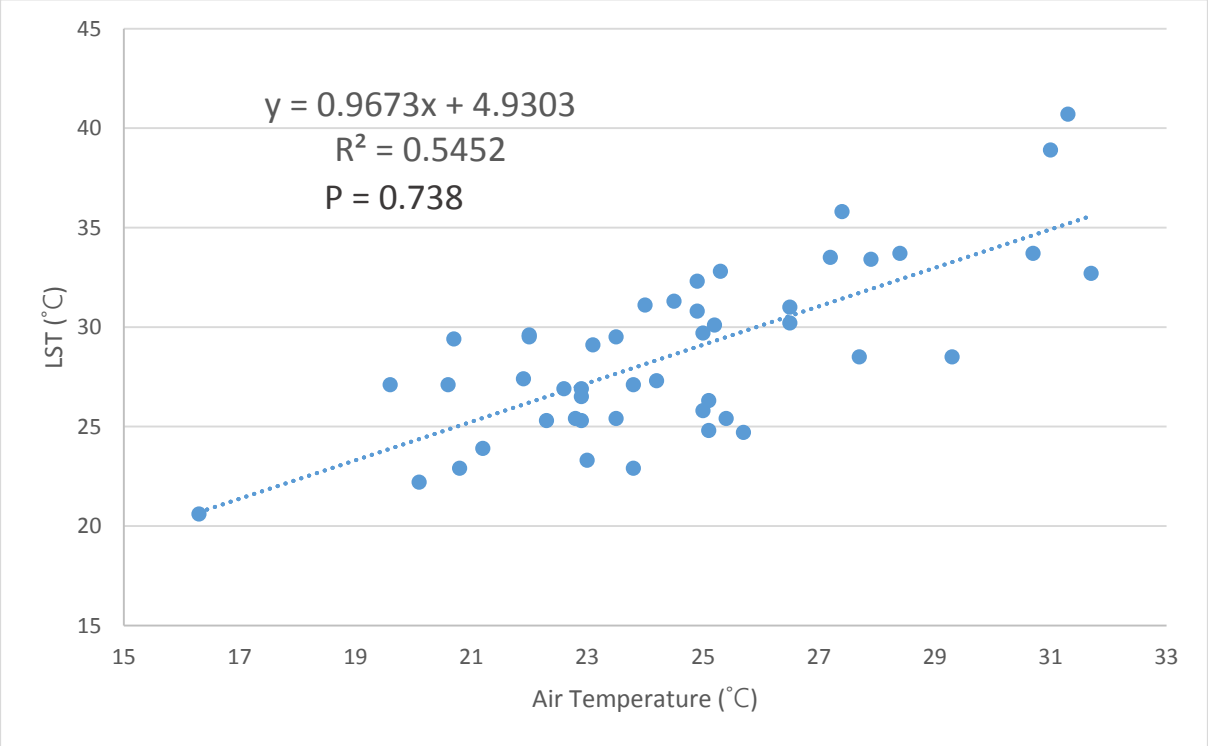

Figure 5.10 LST of pixel location vs. air temperature at weather station of the Pearson International Airport

ASTER thermal band imagery has higher spatial resolution (90 m) and more spectral band (five) than Landsat 5 thermal band image (120 m) and Landsat 8 thermal band images (100 m). With higher spatial and spectral resolution, ASTER images supposed to be preferred in calculating LST while the useful ASTER images are limited not only because higher cloud cover rate and limited data over the GTA but also the smaller coverage area per image which cannot cover the whole GTA by same day imagery. As a result, the only adopted ASTER images are referred as supplementary data. Band 13 of ASTER image is selected to calculate LST which accords with the similar thermal band wavelength of Landsat TM (Band 6), Landsat ETM+ (Band 6) and Landsat 8 (Band 10). SUHI intensity is obtained by subtracting the lowest temperature in rural area from calculated LST. LST maps derived from different date are hard to get the conclusion that which year is more affected by UHI because the limited satellite images per year may introduce bias when considering long term changes. However, the SUHI intensity maps tend to decrease the effect from variable daily temperature by looking for temperature difference. The results of 1984 and 2014 SUHI intensity maps are showed and compared in Figure 5.11. Red colour represents the degree of temperature difference. In areas under strong SUHI phenomenon, the map will still show strong red colour even the temperature is low for that areas, which is the case in Figure 5.11 The temperature associated with the right side map (24.3˚C) is lower than that (26.1˚C) on the left side. From Figure 5.11, it can be concluded that SUHI intensity is high in 2014 because widely distributed red areas are shown on SUHI intensity map of 2014. On the contrary, the map on the left showing very little red part means the SUHI intensity is low in 1984.

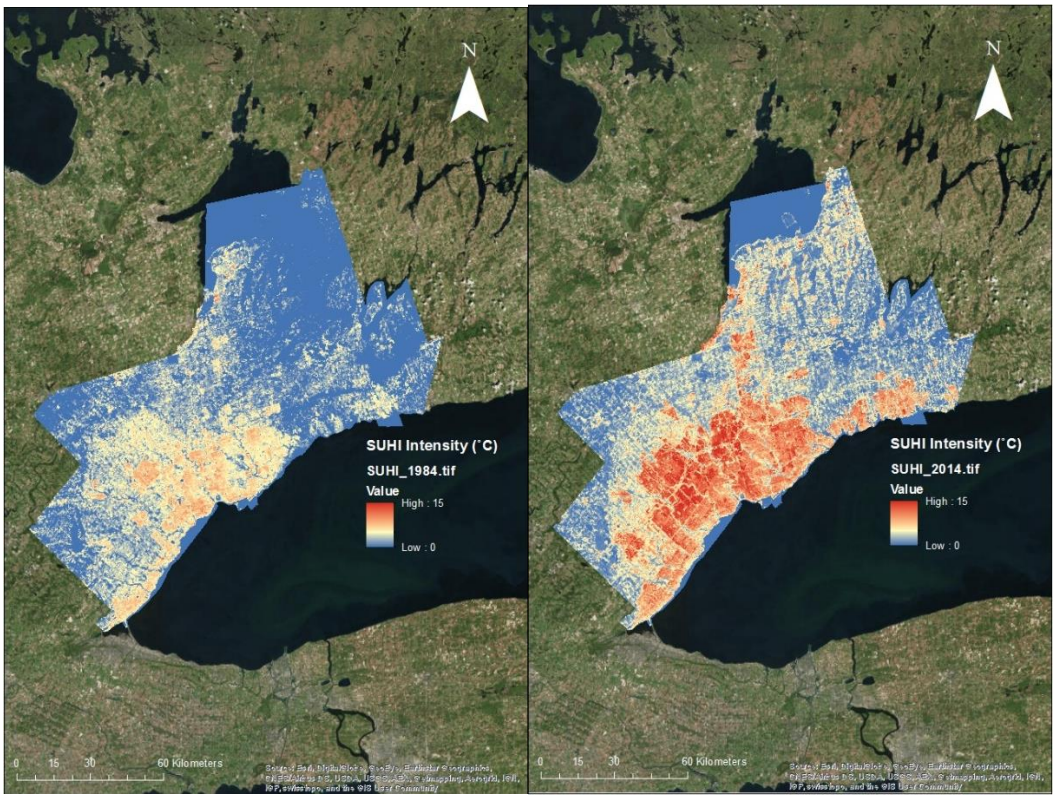

Figure 5.11 SUHI intensity map of the GTA in 1984(left) and 2014(right)

There is another way to present the intensity of SUHI by excluding any rural comparison as most people live in urban areas. This method is proposed by Stewart and Oke (2009) and defines the SUHI using inter-zone temperature difference. By this method, mean LST of the urban core is treated as reference and LST are categorized using thermal thresholds which are 1˚C to 14˚C higher than the mean LST. The result map based on mean LST of downtown Toronto is compared with conventional SUHI map based on rural temperature in Figure 5.12. Presenting of SUHI based on mean LST of the urban core has the superiority in attention to urban thermal distribution. However, this method intends to ignore the function of cool areas within the city boundary according to missing sections on left side map of Figure 5.12. On the contrary, conventional SUHI mapping method has better capacity in detail preserving, but may introduce error, which results from arbitrary selection of rural reference, by overestimation or underestimation of SUHI.

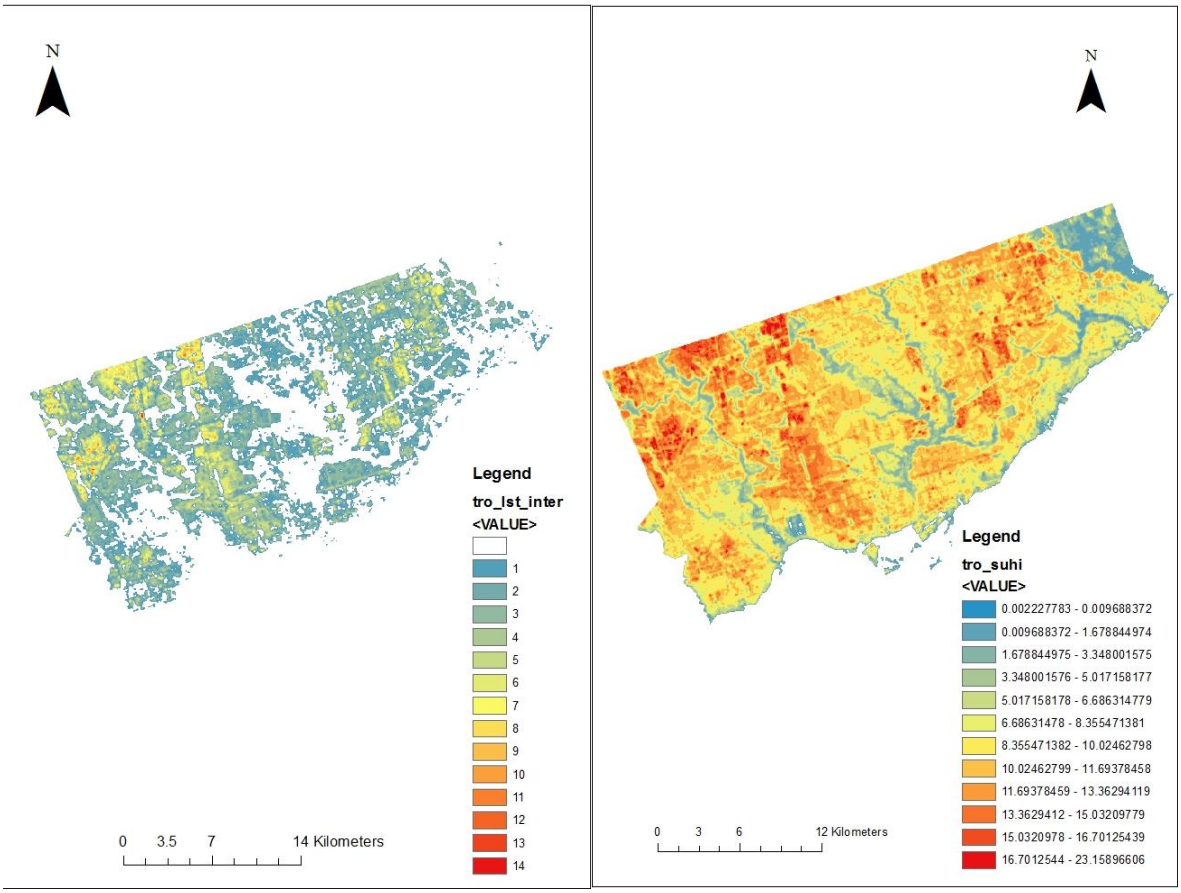

Figure 5.12 SUHI intensity map based on mean LST (left) and based on rural LST (right)

5.2.2 SUHI Characterization

Characterization of SUHI includes providing the basic visualized information like the intensity of SUHI and it could also demonstrate the distribution of SUHI. In the following four sections, SUHI is interpreted spatially regarding to NDVI, land use, population and road network in several individual years between 1984 and 2014.

5.2.2.1 SUHI Characterization Regarding to NDVI

NDVI is widely used to evaluate the vegetation abundance and treated as a factor of SUHI topic as vegetation has the capability to function as alleviator for SUHI. The potential relationship between NDVI and LST is valuable when characterizing SUHI in the GTA. Figure 5.13 shows the

NDVI of the GTA in 1984 and 2014. At the meantime, they are compared with SUHI intensity for corresponding year. As the urbanization effect, more and more green space is replaced by built-up areas. The decreasing of NDVI value and shrink of vegetation extension are observed from the left side maps in Figure 5.13 with more black areas sprawled from urban centre. The SUHI intensity is highlighted by red colour on the right side of Figure 5.13. The increasing areas of high SUHI intensity is agree with the growing low NDVI areas, which shows the potential negative correlation between each other. Table 5.5 describes the statistics of NDVI value and LST for 5 regions within the GTA. Downtown Toronto, the most density urban area in GTA has the lowest mean NDVI and highest mean LST for both years. NDVI and LST maps are compared pixel-by-pixel for the 5 regions and correlation coefficients are summarized in Table 5.6. Downtown Toronto for example, the negative correlation between NDVI and LST presents with significant correlation coefficients of -0.404 for 1984 and -0.678 for 2014 at 0.001 level as shown in Table 5.6. Scatter plots of the downtown Toronto case are shown in Figure 5.14. The downward shape of scatter plots also verifies the negative correlation between NDVI and LST.

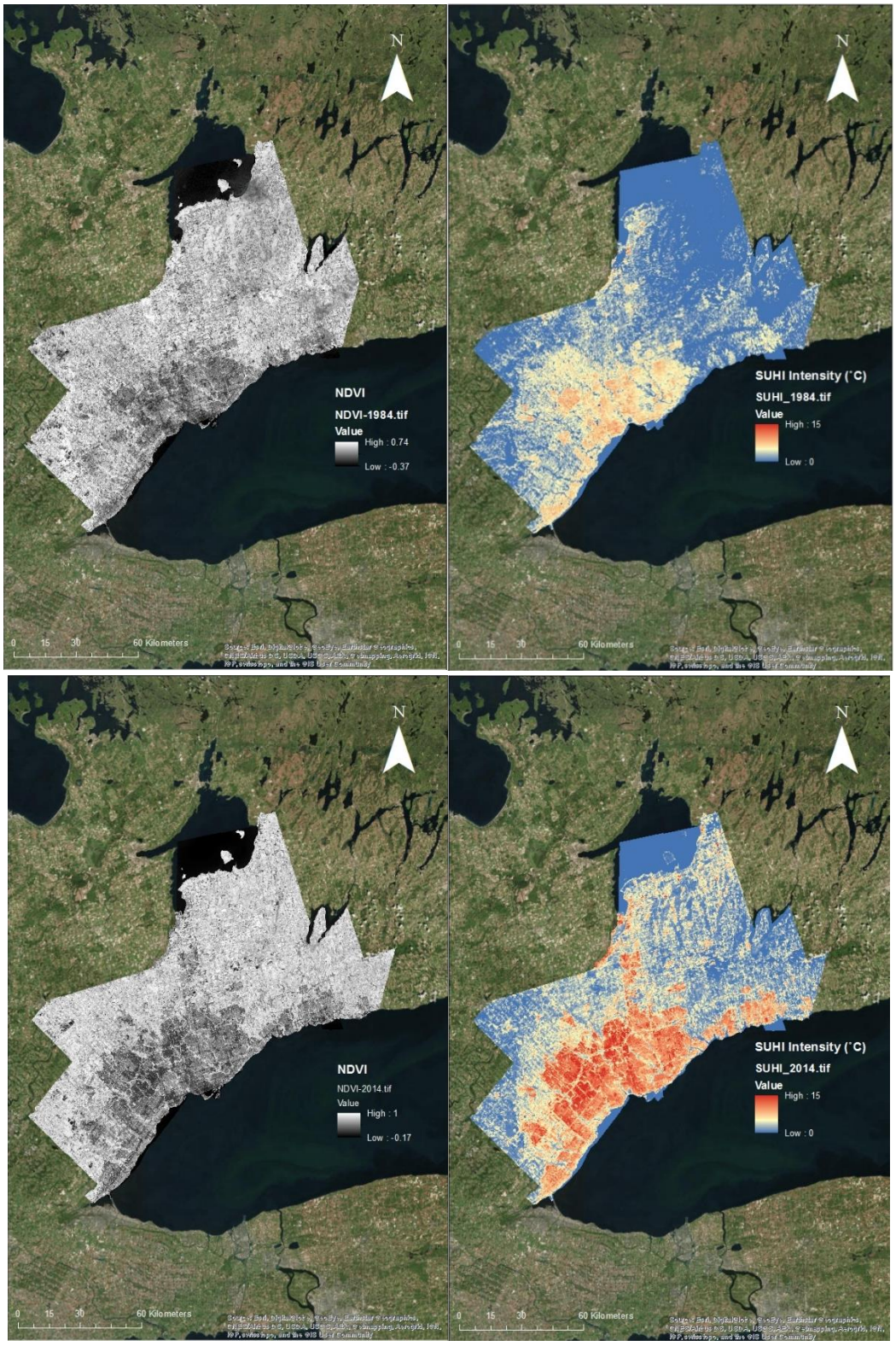

Figure 5.13 NDVI (left) and SUHI (right) intensity map of the GTA in 1984 (up) and 2014 (down)

Table 5.5 Descriptive statistics of NDVI and LST in 5 regions of the GTA in 1984 and 2014

Region	NDVI								LST (K)							
	Min		Max		Mean		STD		Min		Max		Mean		STD	
	1984	2014	1984	2014	1984	2014	1984	2014	1984	2014	1984	2014	1984	2014	1984	2014
Toronto	-0.39	-0.21	0.72	0.64	0.23	0.25	0.18	0.13	276	281	311	316	300	301	4.58	8.82
York	-0.39	-0.20	0.75	0.64	0.35	0.33	0.25	0.19	259	289	308	318	296	297	4.17	4.25
Peel	-0.34	-0.20	0.73	0.64	0.38	0.35	0.18	0.15	278	280	309	317	298	299	3.73	6.14
Durham	-0.33	-0.20	0.74	1.00	0.33	0.37	0.22	0.16	204	284	309	317	293	265	7.60	9.06
Halton	-0.39	-0.20	0.74	0.66	0.42	0.38	0.18	0.13	281	279	310	316	298	298	3.64	6.32

Table 5.6 Correlation coefficients between NDVI and LST of 5 regions of the GTA in 1984 and 2014 (*significant at 0.001)

Year	NDVI/LST (Toronto)	NDVI/LST (York)	NDVI/LST (Peel)	NDVI/LST (Durham)	NDVI/LST (Halton)
1984	-0.404*	-0.424*	-0.393*	-0.415*	-0.304*
2014	-0.678*	-0.756*	-0.789*	-0.529*	-0.653*

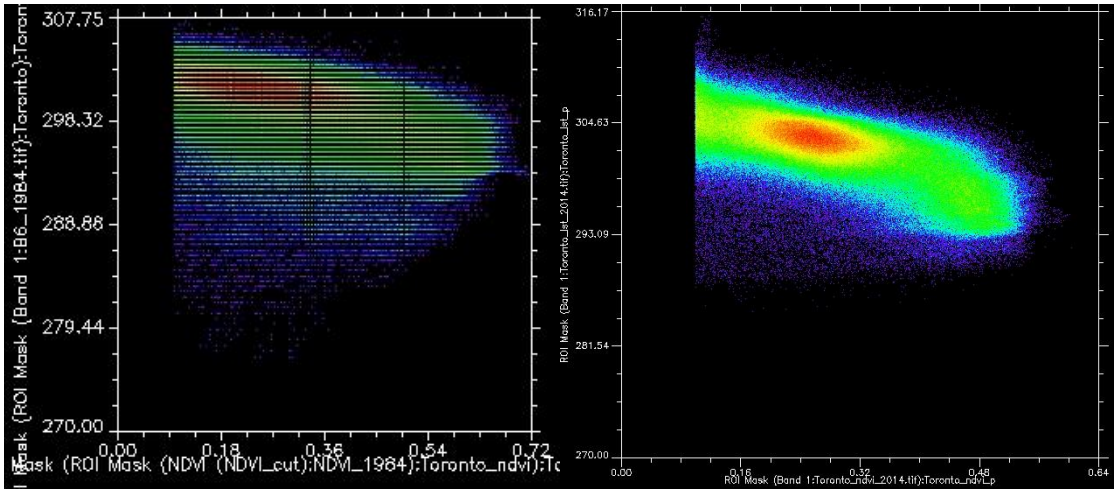

Figure 5.14 2D-Scatter plots (NDVI vs. LST) for downtown Toronto in 1984 (left) and 2014 (right)

5.2.2.2 SUHI Characterization Regarding to Land Use

Land use shapefile of the GTA is integrated with the LST map to explore the underlying SUHI feature. Land use categories are classified as commercial, government and institution, open area, parks and recreation, residential, resource and industrial and water body according to Ontario Ministry of Natural Resources. Figure 5.15 shows the sample shapefile of land use in 2008. From Figure 5.15, we can find that land use type is not equally distributed across the GTA. The Land use types associated with human activities extends from the urban centre to the north and to the east and west along the Ontario Lake.

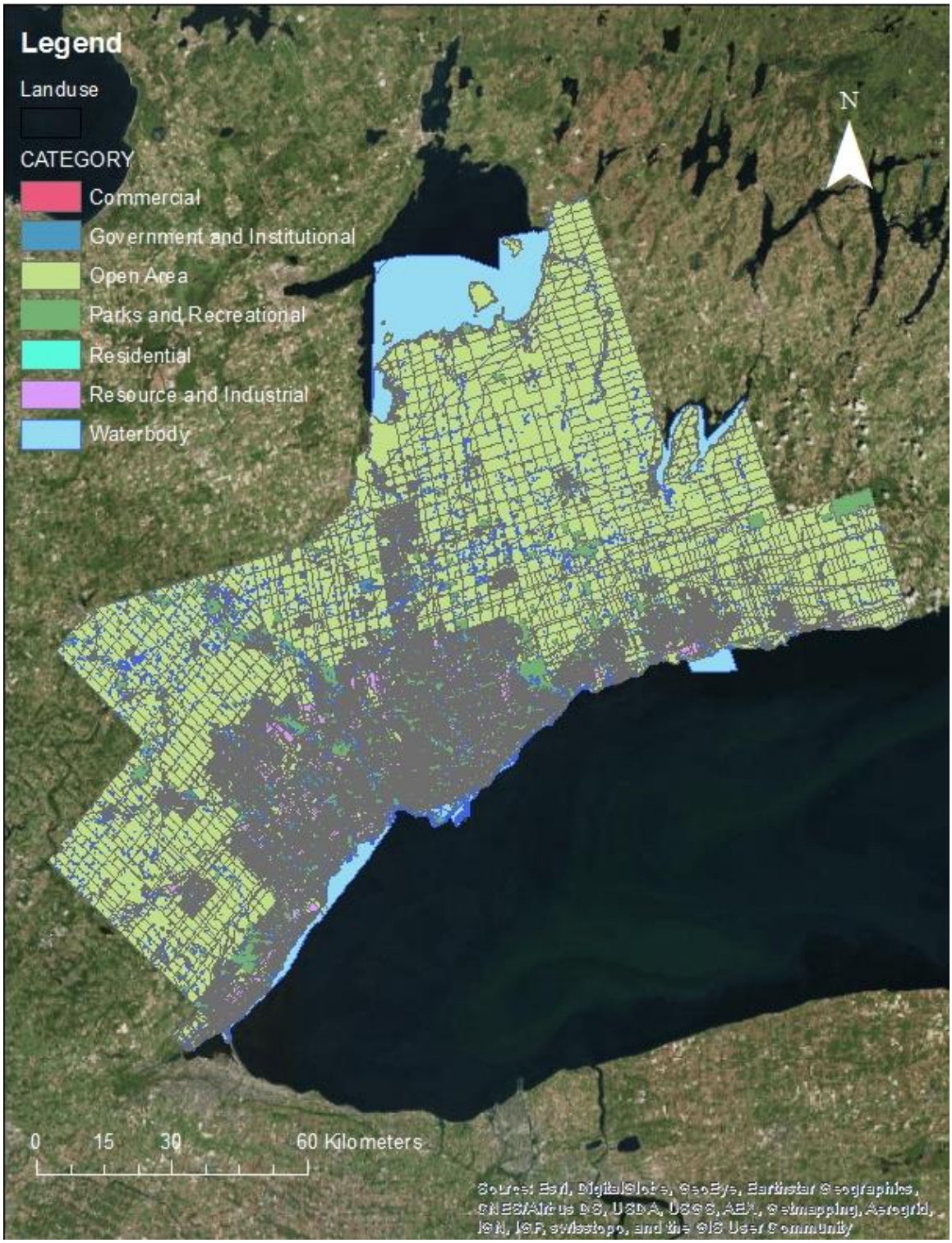

Figure 5.15 Land use map of the GTA, 2008

In Figure 5.16, LST map is overlaid above land use map and typical areas are selected for further discussion in Figure 5.16.

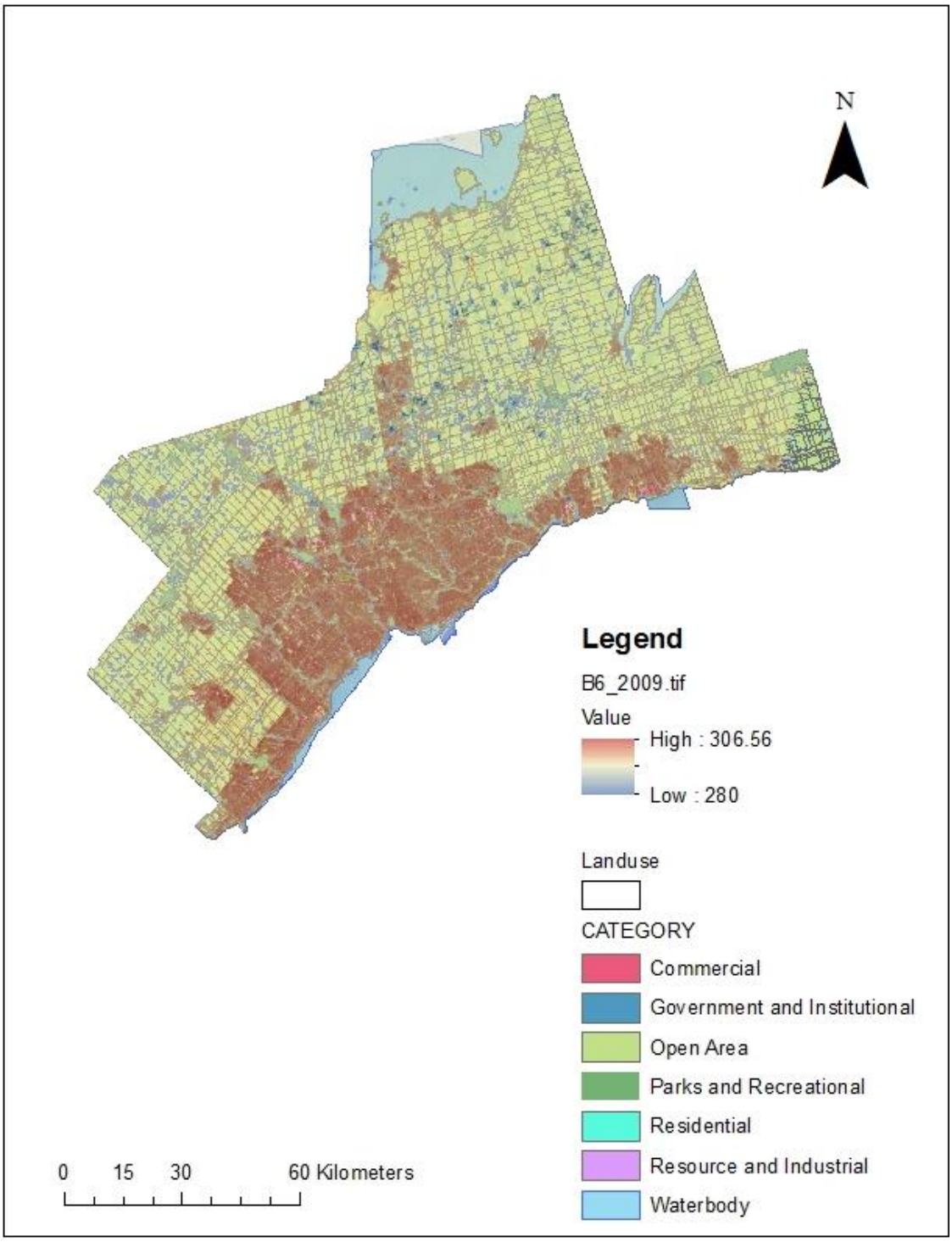

Figure 5.16 LST map overlays on top of the land use map of the GTA

From the scale of Figure 5.16, it is hard to tell the connection between land use type and LST, however, the hot areas tend to distribute on centre urban areas where commercial and residential type land use are highly centralized. In order to further understand how land use types associate with LST, mean LST of each land use type is estimated for the GTA in 2009 and 2014 and listed in Table 5.7.

Table 5.7 Mean LST based on different land use type for the GTA in 2009 and 2014

Land Use Type	2009			2014		
	Area (km^2)	Mean (K)	STD	Area (km^2)	Mean (K)	STD
Waterbody	525.8	289.81	11.4	454.3	308.34	63.5
Open Area	5010.1	287.59	39.6	5012.0	317.32	63.5
Parks and Recreational	452.6	293.76	12.5	452.7	313.34	66.5
Government and Institutional	107.1	297.65	3.1	107.2	313.56	5.6
Residential	1201.6	298.32	4.5	1201.6	316.26	23.4
Resource and Industrial	312.1	297.64	18.6	312.1	317.95	38.1
Commercial	40.9	300.17	2.1	40.9	317.07	6.4

Commercial areas typically have higher mean LST compared to parks according to Table 5.7. The possible explanations is commercial areas have large amount of impervious layers such as parking lots and roofs which absorb and store the heat while parks are covered with vegetation or water which cools the surface by evaporation.

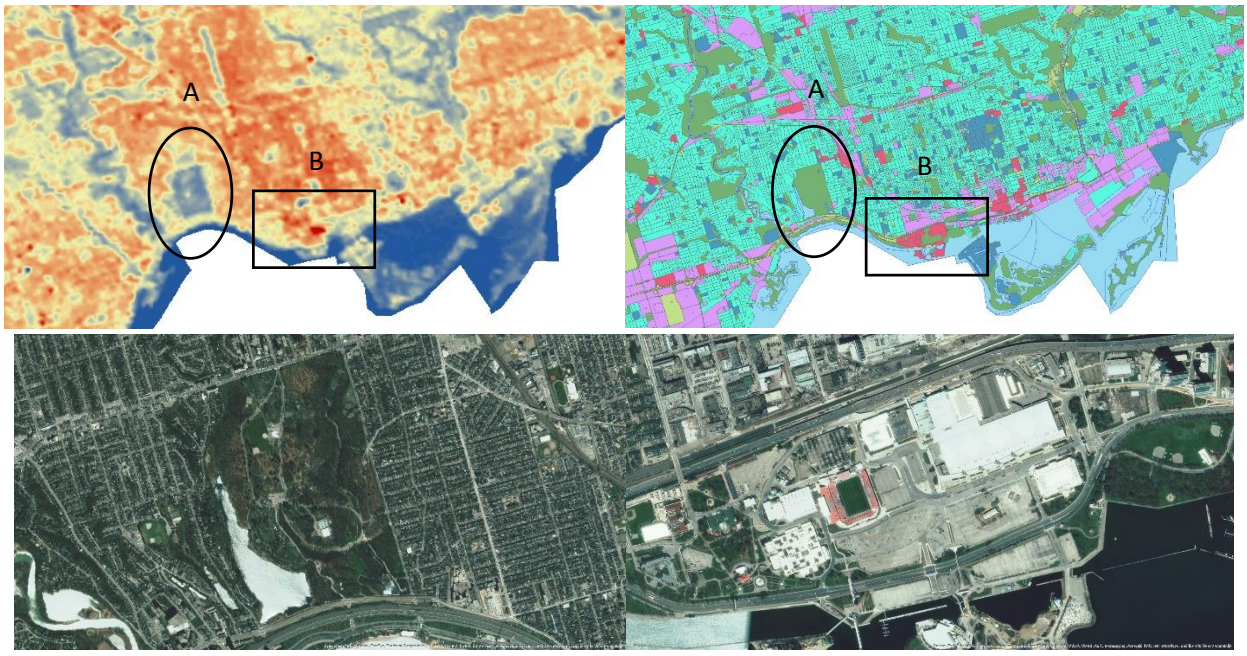

A B

Figure 5.17 Sample cool (A) and hot (B) spots in the LST map of the GTA

As shown in Figure 5.17, the left cool blue part A is the High Park with temperature lower than mean LST and the right red portion B is proved as commercial district where the Canadian National Exhibition (CNE) is located with temperature higher than mean LST. From two satellite images in Figure 5.17, it can be found that parks with high vegetation coverage helps to reduce the surface temperature while commercial areas with lots of impervious surfaces like bare building roofs and parking lots will increase the surface temperature. In generally, temperature difference in this case can reach as much as 15˚C. Another characteristic scenario is described in Figure 5.18 marked by area A and B. Both A and B are classified as Resource and Industrial in land use shapefile. By referring to OpenStreetMap and Google maps which are very helpful websites to figure out the accurate landmark information, A is Ford Canada Assembly Complex and B are Holcim Canada and Petro-Canada Lubricants Plant. The energy consumption is generally higher for these large factories compared with residential areas. Meanwhile, the industrial waste gas emission is

inevitable. Large amount of heat as the appurtenance of emission is brought to the surrounding environment during the factory operation.

Figure 5.18 Thermal behaviors of factories in LST map of the GTA

As the biggest source of air pollution in Canada before, coal-burning power plants has been closed one after another since 2003. As the last station in the GTA, the Lakeview Generating Station, which located in Mississauga was demolished in 2006. Figure 5.19 compares the image-based LST for that particular location (43˚34’16” N, 79˚33’6” W) before and after the shutting down of power plants in 2006. Two images of Landsat TM are compared with similar weather condition at acquisition time. Detailed information is shown in Figure 5.19. The bright white colour presents the temperature level in these two pictures and the up picture is much brighter than the one below

it. It means the temperature is higher for the up picture. By calculating the LST for two images, it can be found that the calculated LST agrees with the inference. The LST drops from 28.85˚C to 20.58˚C after the demolishment of power plant in 2006.

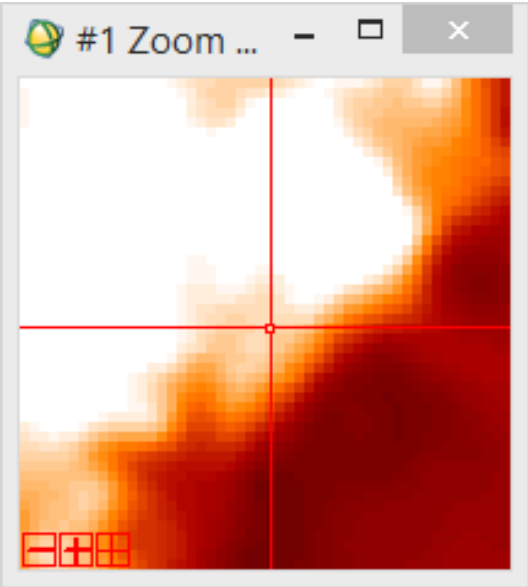

Sensor Type: Landsat TM

Acquisition data & time: Aug 18, 2002 @10:30am

Imagery resolution: 120m

Air temperature: 25˚C

Wind speed: 25km/h

Humidity: 28%

LST: 28.85˚C

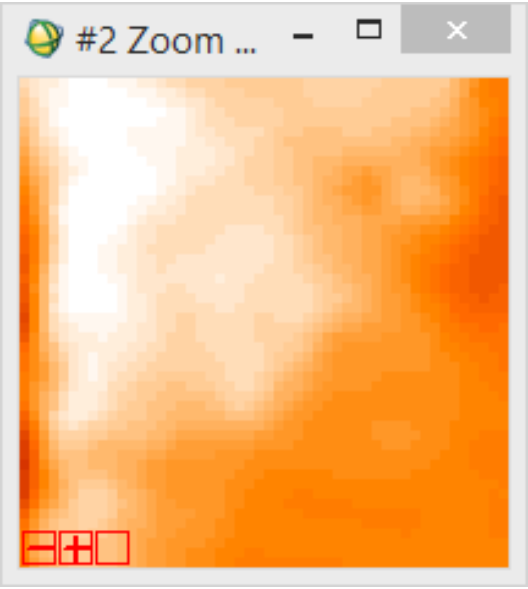

Sensor Type: Landsat TM

Acquisition data & time: Aug 21, 2009 @10:30am

Imagery resolution: 120m

Air temperature: 24.9˚C

Wind speed: 23km/h

Humidity: 31%

LST: 20.58˚C

Figure 5.19 Compare of LST before (up) and after (down) power plant demolished at 2006

5.2.2.3 SUHI Characterization Regarding to Population

SUHI is not only influenced by "real" heat form but also can be shaped by the degree of human activities. Therefore, the population density as indirect measurement of potential human activities could be connected with SUHI characterization. 2011 GTA census of population data is mapped in Figure 5.20 covering the whole GTA and in Figure 5.21 covering downtown Toronto. Population shows low density in the rural area but is highly concentrated in the city centre and along the lake shore based on Figure 5.20 and Figure 5.21. Population density is classified by 6 classes and mean LST of each class is calculated based on August 27, 2011 imagery. The result is shown in Table 5.8.

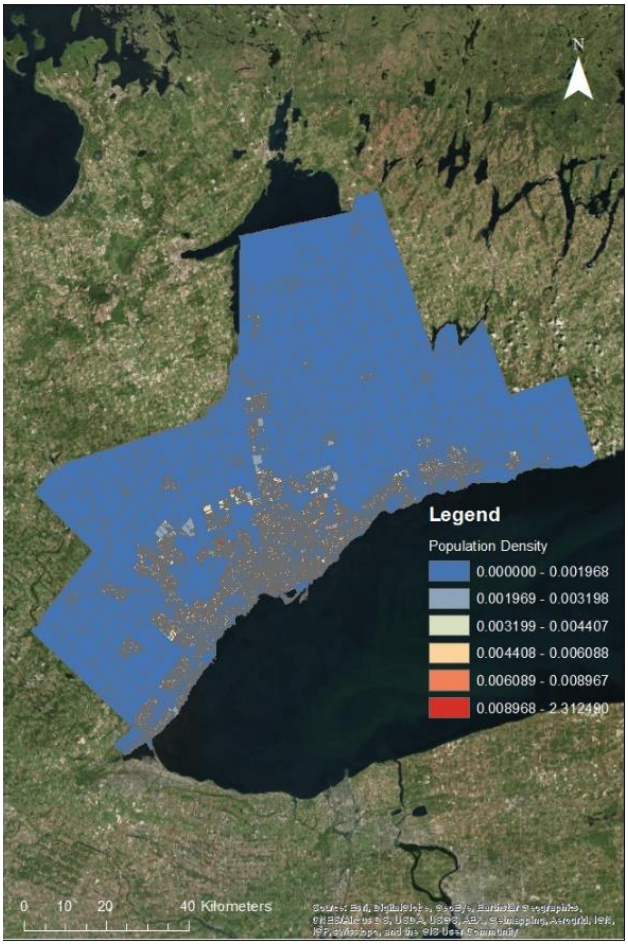

Figure 5.20 GTA population density in Census 2011

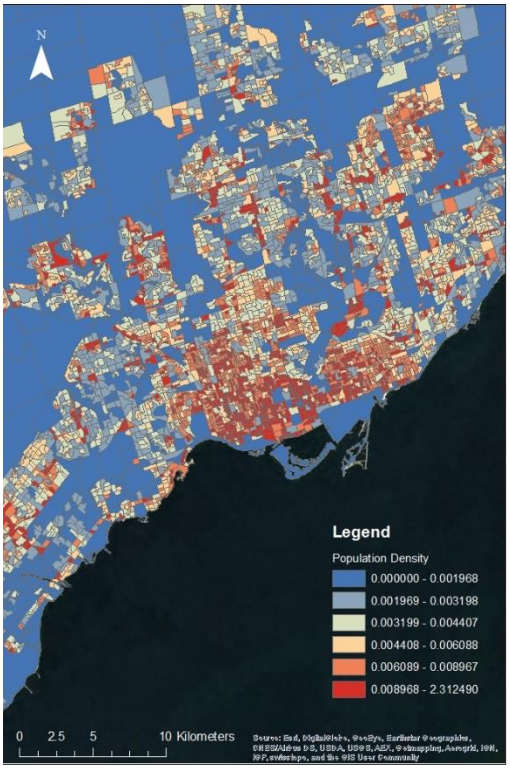

Figure 5.21 Downtown Toronto population density in Census 2011

Table 5.8 Relation between population density and mean LST in 2011

Classes	Population Density (People/m^2)	Mean LST (K)	STD
1	< 0.002	299.3356	1.4456
2	0.002 to 0.004	302.0505	2.2545
3	0.004 to 0.006	303.0914	1.4988
4	0.006 to 0.008	304.1151	2.3407
5	0.008 to 0.010	304.2345	2.3063
6	> 0.010	305.0698	2.4667

Table 5.8 shows that as the increase of population density, mean LST is also increased from 299K to 305K. In Figure 5.22, it shows proportional relationship between the population density and the LST. Accordingly, it can be concluded that, the population distribution will affect the SUHI of the city by contributing to the increase of LST.

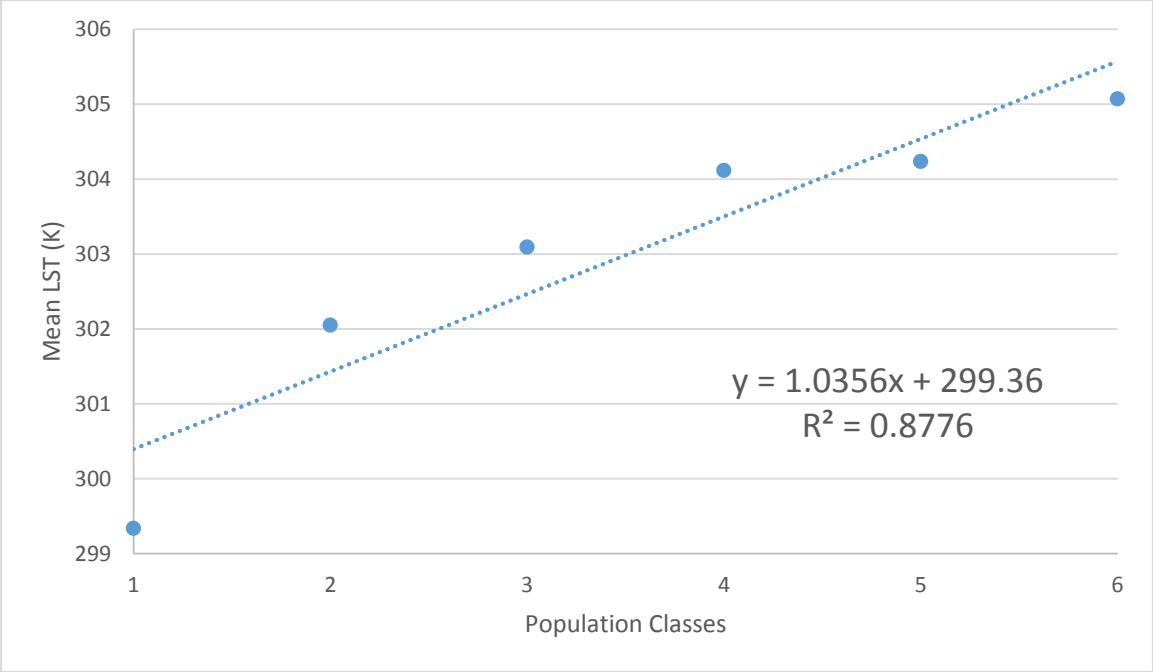

Figure 5.22 Population density by classes vs. mean LST in 2011

5.2.2.4 SUHI Characterization Regarding to Road Network

Last but not least, SUHI is characterized by considering transportation conditions in the GTA since many studies have suggested that vehicle exhaust emission could promote greenhouse gas emission which is acknowledged to be primary contribution to the SUHI.

Figure 5.23 shows the increasing of road coverage of the GTA from 2006 to 2014 by red lines. New roads are mainly built around the urban edge and inside the urban centre. It is combined with the LST map and the consequential result is mapped in Figure 5.24.

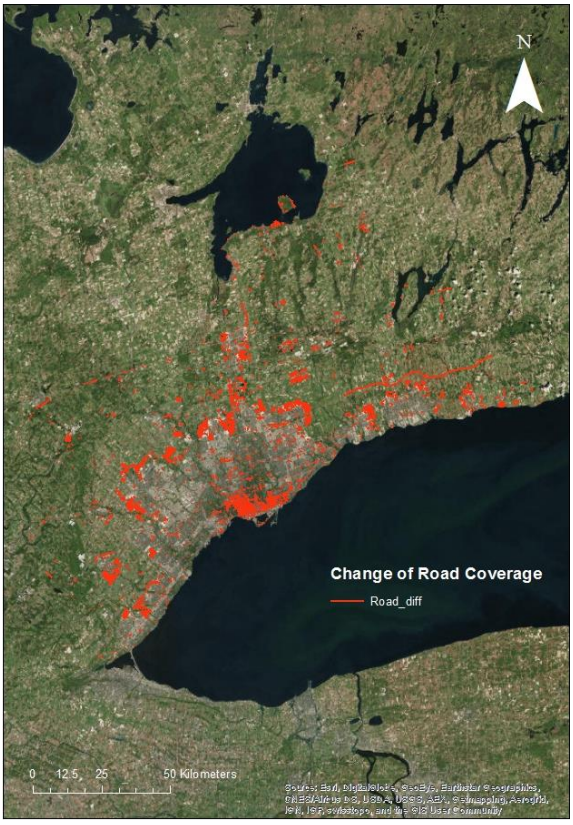

Figure 5.23 Change of road coverage in the GTA from 2006 to 2014

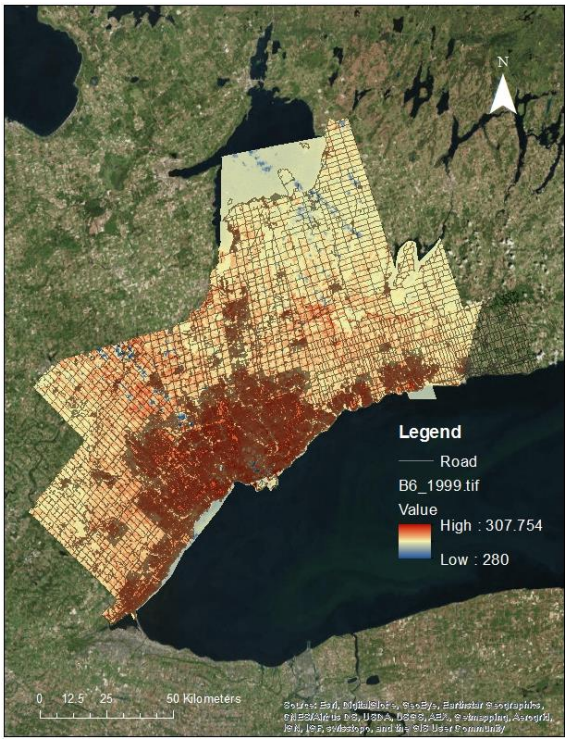

Figure 5.24 Overlay of the LST map on the road network of the GTA in 2014

According to Figure 5.24, LST enhances as the increasing of road network density. In allusion to the land use standpoint from sections above, it is clear to conclude that SUHI spreads from the city core. From another point of view, which is the viewpoint of road network, it is forceful to say that SUHI extends along the main road network depends on its geography appearance. When zoom in the thematic map, it can be found that main road network such as big street and Hwy are distinguished from background. The high traffic volume generates more heat than nearby low level streets. The relation between road and mean LST is pointed out in Table 5.9.

Table 5.9 Relation between roads and mean LST along the GTA road in 2006 and 2014

Road	Mean LST (K)	
	2006	2014
S (<40 km/h)	305.7	296.9
M (40-60 km/h)	307.3	302.0
C (60-80 km/h)	303.2	296.2
H (>80 km/h)	306.9	300.5

The road is classified based on the speed limitation and according to city of Toronto. S road is defined as local road with low traffic volume and low traffic speed; M road is defined as major road within the city with high traffic volume and medium traffic speed; C road is defined as country road with medium to low traffic volume and high traffic speed; H road is defined as highway with high traffic volume and high traffic speed. M roads account for the most of the mean LST and H roads rank second for both years. It can be conclude that high traffic volume may increase the LST and lower traffic speed will promote the SUHI under similar traffic volume situation because the vehicles usually consume more fuel under poor urban traffic condition.

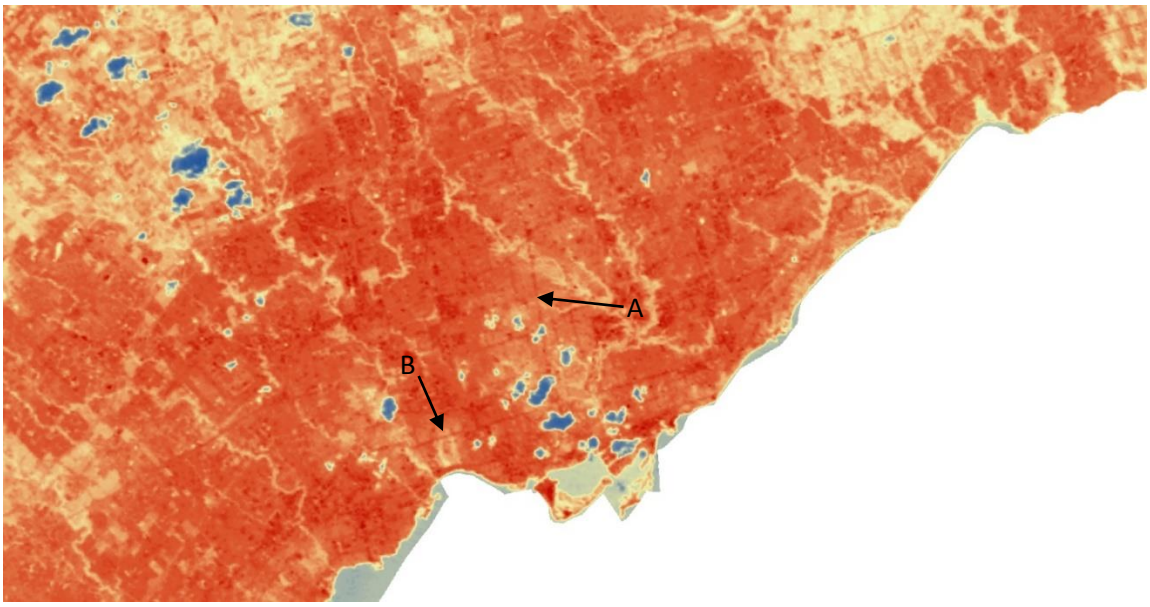

Figure 5.25 Yonge St. and Bloor St. shown in the LST map of the GTA

Two dark red lines are very remarkable in Figure 5.25 even they are surrounded by most bustling downtown Toronto. The road A which passes through downtown Toronto from south to north is Yonge Street. The traffic volume in a single day of one intersection at Yonge Street can reach 129,704 according to data collected by City of Toronto Transportation Services. This street was the longest street in the world and it is one of the most heavily used road due to its important geographical function which connects the downtown Toronto and uptown Toronto, even to the north developing region. The road B, Bloor Street, plays the same important role in Toronto. It connects the most primary commercial district and financial district from west to east. However, instead of praising the driven force to economy from these two street, concerns should be placed for the SUHI caused by high traffic volume within the city. High traffic also brings hidden threat to the rural areas as shown in Figure 5.26. Road A in Figure 5.26 is still noticeable compared with nearby rural road for high surface temperature along the road when outside the city boundary. Road A is Hwy 404 according to its position. A vast of traffic goes north through this Hwy and makes it a “hot” line in this case.

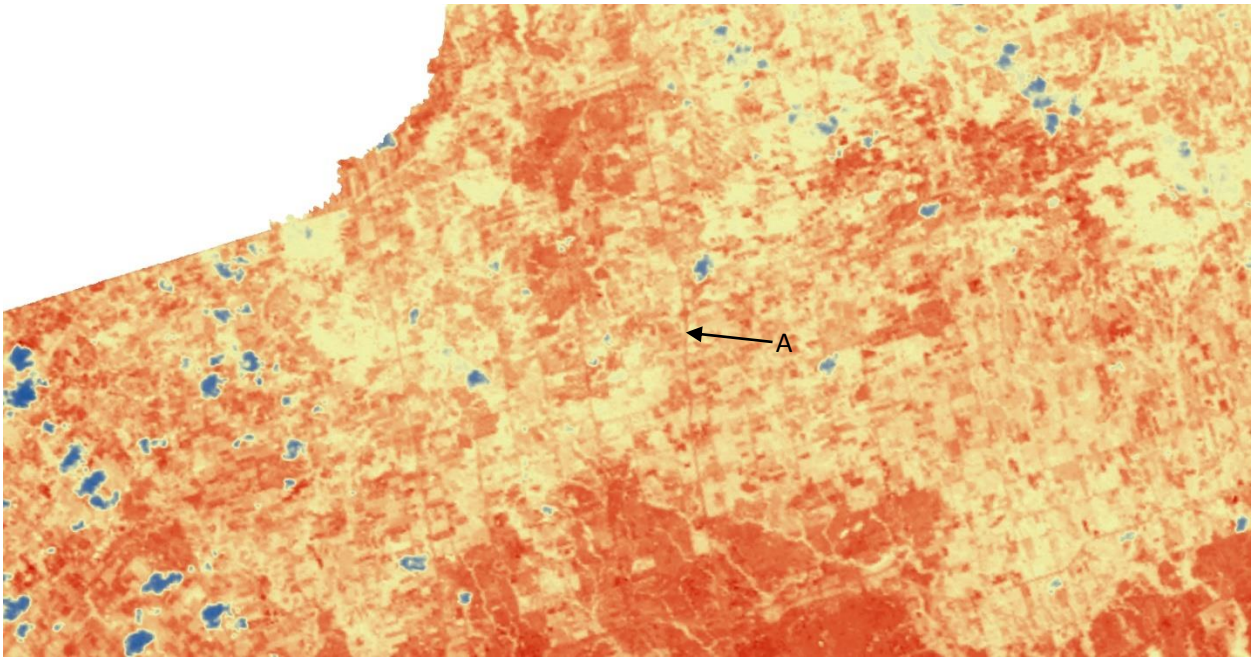

Figure 5.26 Major street shown in the LST map

Chapter 6

Conclusions and Recommendations

In this study, annual mean air temperature trend and characteristic of annual and seasonal UHI have been explored successfully in the GTA by analyzing historical temperature records from local weather stations. Additionally, long-term thermal band satellite images are applied to characterise SUHI in the GTA regarding to different urban characteristics such as vegetation, land use, population and road network. In this chapter, major findings, meaningfulness and contribution of this study will be explained. Meanwhile, limitations and insufficiency in this study will be pointed out as well. Finally, future studies will be composed and suggested.

6.1 Key Findings

One of the main objectives of this study is to discover the trend of historical air temperature data for the past 30 years. The other objective is to characterise the SUHI for the GTA by using satellite images.

6.1.1 Historical Data Trend

Non-parametric statistical methods such as Mann-Kendall test and Kendall's tau are applied to 30 years weather stations' data from 1984 to 2014. The result of annual mean temperature trend test indicates a mild increasing trend for downtown Toronto and the very far rural weather stations. However, significant increasing trend at 0.05 level for annual mean temperature is presented at the weather stations such as the Pearson International Airport and Richmond Hill where experiencing high pace development in recent decades. Despite the variation of significant level for air temperature trend at different locations, the annual UHI intensity of downtown Toronto is

increased generally with increased extreme value during the past five years. On the contrary, the seasonal UHI intensity fluctuates without significant trend in the downtown Toronto from 1984 to 2014. The contribution to the study in this part is to include the latest meteorological data and reveal the slowdown of temperature raise in downtown Toronto. In other words, the rapid heating area is shifted from downtown Toronto to the Pearson International Airport area and Richmond Hill according to the trend test.

6.1.2 SUHI Mapping

Landsat thermal band images were selected as its stable performance and availability of long term images. LST of weather stations in downtown Toronto and the Pearson International Airport was calculated from thermal band satellite images and compared with weather stations' historical temperature data. The result shows high correlation between image-based land surface temperature and weather stations' data, which implies the potential to convert LST to air temperature. After combining image-based LST map with NDVI, land use data, population density information and road network shapefile, SUHI is characterised accordingly. For instance, high vegetation covered areas are usually lower in temperature. Increasing urban impervious level has seriously raised local surface temperature where commercial and industrial land use types are commonly under such situation. Moreover, the SUHI intensity is decreased away from main roads and presents urban-centered radiate shape and distribution. In addition, main roads with high traffic volume but low speed were conspicuous among the images by showing a linear shape of SUHI along the road networks. A typical example is the Yonge Street which presented much higher temperature than its surrounding areas due to its high traffic volume. Finally, by connecting census data to LST, it shows directly connection between population density and LST in the GTA with high correlation

coefficient. The contribution to the study in this part is to take the whole GTA as study area which covers more extensive area as the requirement of urban sprawl. Furthermore, long term satellite images were selected from 1984 to 2014 in order to characterised SUHI based on data like NDVI, land use, population and road network. In this way, it brings more unique perspectives instead of pursuing the universal image processing algorithm fanatically.

6.2 Limitations of the Study

This study relied on the weather stations' historical meteorological data to evaluate temperature trend. Hence the reliability and accuracy of the data was very crucial. However, some situations were unpredictable and inevitable during the actual operation, such as missing of data, relocation of measurement equipment, cancelation of weather station and modification of record interval. All of these effect may decrease the reliability of conclusion.

From the remote sensing perspective, Landsat data provide long-term records downloadable directly from the USGS website, which makes it a better choice for this study. However, Landsat thermal band data with 60m to 120m resolution are too coarse to represent the features of SUHI accurately, especially in high density urban areas. Besides, images covering the GTA were only captured in the day time every 16 days. The low temporal resolution makes it not applicable for long term trend analysis. In addition, the study of night time SUHI which could be representative was hardly possible in this study due to no data available during the night.

When processing satellite images, LST was calculated from on board digital value according to a very basic and conservative image-based method. Although multiple methods have been

introduced to convert LST to air temperature, which is more reasonable when compared with temperature data from weather stations, there has been no golden rule to apply so far. Even some compromised method can achieve quite good result, but requirement of detailed meteorological parameters was hard to meet in this study with historical data dates back to 1984.

6.3 Future Studies

Based on the significances and limitations mentioned above, some future works are suggested here. As the current work in this study is mainly based on qualitative analysis and imagery interpretation, future studies may focus on the development of quantitative analysis regarding to SUHI. Self-collecting high quality in site data such as minutely air temperature and surface temperature, global solar radiation, atmospheric transmission and upwelling radiance can be added to the dataset as supplementary data for official station records. With detailed atmosphere data, the accuracy of calculated LST will be improved by applying advanced image processing algorithms such as split-window algorithm and mono-window algorithm. With robust LST data, the next step is to evaluate the effect from each factor. In current study, only the factors from urbanization are considered. However, weather and climate factors also influence the SUHI. By integrating all of this factors into the quantitative analysis model after detailed study of each factor, it could be possible to analyze and predict the SUHI with multicriteria decision analysis using a GIS without subjective guess of weight for each factors. Another direction of future study may take into account the bias between LST and air temperature. As the high correlation between LST and air temperature in current study, future works can be done regarding to convert LST to air temperature based on some sophisticated numerical and physical models such as energy balance models, three-dimensional simulations and Gaussian models.

References

Ao, K. F., & Ngo, H. T. M. (2000). GIS Analysis of Vancouver's Urban Heat Island, 2006. http://www.geog.ubc.ca/courses/klink/g470/class00/kfao/abstract.html.

Argaud, L., Ferry, T., Le, Q.-H., Marfisi, A., Ciorba, D., Achache, P., Ducluzeau, R., Robert, D. (2007). Short- and long-term outcomes of heatstroke following the 2003 heat wave in Lyon, France. *Archives of Internal Medicine*, *167*(20), 2177–2183.

Arnfield, a. J. (2003). Two decades of urban climate research: A review of turbulence, exchanges of energy and water, and the urban heat island. *International Journal of Climatology*, *23*(1), 1–26.

Brazel, A., Selover, N., Vose, R., & Heisler, G. (2000). The tale of two climates - Baltimore and Phoenix urban LTER sites. *Climate Research*, *15*(2), 123–135.

Ca, V. T., Asaeda, T., & Abu, E. M. (1998). Reductions in air conditioning energy caused by a nearby park. *Energy and Buildings*, *29*(1), 83–92.

Camilloni, I., & Barros, V. (1997). On the urban heat island effect dependence on temperature trends. *Climatic Change*, *37*(4), 665–681.

Carnahan, W. H., & Larson, R. C. (1990). An analysis of an urban heat sink. *Remote Sensing of Environment*, *33*(March), 65–71.

Choi, Y.-Y., Suh, M.-S., & Park, K.-H. (2014). Assessment of Surface Urban Heat Islands over three megacities in East Asia using Land Surface Temperature data retrieved from COMS. *Remote Sensing*, *6*(6), 5852–5867.

Çiçek, I., & Doğan, U. (2006). Detection of urban heat island in Ankara , Turkey. *Il Nuovo Cimento*, *29*(4), 399–409.

Christen, A., & Vogt, R. (2004). Energy and radiation balance of a central European City. *International Journal of Climatology*, *24*(11), 1395–1421.

Coutts, A., Beringer, J., & Tapper, N. (2010). Emissions: Implications for the Development of Policies for Sustainable Cities. *Urban Policy and Research*, *28*(1), 27–47.

Craig, C. D., & W. P. Lowry. (1972). Reflections on the urban albedo. *Conf. on the Urban Environment and Second Conf. on Biometeorology*, Philadelphia, PA, Amer. Meteor. Soc., 159–164.

Curriero, F. C., Heiner, K. S., Samet, J. M., Zeger, S. L., Strug, L., & Patz, J. a. (2002). Temperature and mortality in 11 cities of the eastern United States. *American Journal of Epidemiology*, *155*(1), 80–87.

D ȧz, S., Hector, A., & Wardle, D. a. (2009). Biodiversity in forest carbon sequestration initiatives: not just a side benefit. *Current Opinion in Environmental Sustainability*, *1*(1), 55–60.

Dixon, P. G., & Mote, T. L. (2003). Patterns and Causes of Atlanta's Urban Heat Island–Initiated Precipitation. *Journal of Applied Meteorology*, *42*(9), 1273–1284.

EPA's Report on the Environment (EPA). (2008). U.S. Environmental Protection Agency, Washington, D.C., EPA/600/R-07/045F (NTIS PB2008-112484), 2008.

Fabrizi, R., Bonafoni, S., & Biondi, R. (2010). Satellite and ground-based sensors for the Urban Heat Island analysis in the city of Rome. *Remote Sensing*, *2*(5), 1400–1415.

Finkenbine, J. K., Atwater, J. W., & Mavinic, D. S. (2000). Stream health after urbanisation. *Journal of the American Water Resources Association*, *36*(5), 1149–1160.

Fouillet, a., Rey, G., Laurent, F., Pavillon, G., Bellec, S., Guihenneuc-Jouyaux, C., … Hémon, D. (2006). Excess mortality related to the August 2003 heat wave in France. *International Archives of Occupational and Environmental Health*, *80*(1), 16–24.

Gaffin, S. R., Rosenzweig, C., Khanbilvardi, R., Parshall, L., Mahani, S., Glickman, H., … Hillel, D. (2008). Variations in New York city's urban heat island strength over time and space. *Theoretical and Applied Climatology*, *94*(1-2), 1–11.

Gallo, K. P., McNAB, a. L., Karl, T. R., Brown, J. F., Hood, J. J., & Tarpley, J. D. (1993). The use of a vegetation index for assessment of the urban heat island effect. *International Journal of Remote Sensing*, *14*(11), 2223–2230.

Goetz, S. J., Halthore, R. N., Hall, F. G., & Markham, B. L. (1995). Surface temperature retrieval in a temperate grassland with multiresolution sensors. *Journal of Geophysical Research*.

Grimmond, C. S. B. (2006). Progress in measuring and observing the urban atmosphere. *Theoretical and Applied Climatology*, *84*(1-3), 3–22.

Helsel, D. R., & Hirsch, R. M. (2002). Statistical Methods in Water Resources. *Technometrics*, *36*(3), 522.

Holmer, B., Thorsson, S., & Eliasson, I. (2007). Cooling rates, sky view factors and the development of intra-urban air temperature difference. *Geografiska Annaler, Series A: Physical Geography*, *89 A*(4), 237–248.

Howard, L. (1833). *The Climate of London*. London: International Association for Urban Climate.

Tran, H., Uchihama, D., Ochi, S., & Yasuoka, Y. (2006). Assessment with satellite data of the urban heat island effects in Asian mega cities. *International Journal of Applied Earth Observation and Geoinformation*, *8*(1), 34–48.

Ichinose, T., Shimodozono, K., & Hanaki, K. (1999). Impact of anthropogenic heat on urban climate in Tokyo. *Atmospheric Environment*, *33*(24-25), 3897–3909.

Imhoff, M. L., Zhang, P., Wolfe, R. E., & Bounoua, L. (2010). Remote sensing of the urban heat island effect across biomes in the continental USA. *Remote Sensing of Environment*, *114*(3), 504–513.

Jimenez-Munoz, J. C., Cristobal, J., Sobrino, J. a., Sòria, G., Ninyerola, M., & Pons, X. (2009). Revision of the single-channel algorithm for land surface temperature retrieval from landsat thermal-infrared data. *IEEE Transactions on Geoscience and Remote Sensing*, *47*(1), 339–349.

Karl, T. R., Diaz, H. F., & Kukla, G. (1988). Urbanization: Its Detection and Effect in the United States Climate Record. *Journal of Climate*, *11*(1), 1099–1123.

Keatinge, W. R., Donaldson, G. C., Cordioli, E., Martinelli, M., Kunst, a E., Mackenbach, J. P., … Vuori, I. (2000). Heat related mortality in warm and cold regions of Europe: observational study. *BMJ (Clinical Research Ed.)*, *321*(7262), 670–673.

Kim, H. H. (1992). Urban heat island. *International Journal of Remote Sensing*, *13*(12), 2319–2336.

Klok, L., Zwart, S., Verhagen, H., & Mauri, E. (2012). The surface heat island of Rotterdam and its relationship with urban surface characteristics. *Resources, Conservation and Recycling*, *64*, 23–29.

Krause, C. W., Lockard, B., Newcomb, T. J., Kibler, D., Lohani, V., & Orth, D. J. (2004). Predicting influences of urban development on thermal habitat in a warm water stream. *Journal Of The American Water Resources Association*, *40*(6), 1645–1658.

Kusaka, H., Kimura, F., Hirakuchi, H., & Mizutori, M. (2000). The Effects of Land-Use Alteration on the Sea Breeze and Daytime Heat Island in the Tokyo Metropolitan Area. *Journat of the Meteorotogical Society of Japan*, *78*(4), 405–420.

Landsberg, H. E. (1970). Man-Made Climatic Changes: Man's activities have altered the climate of urbanized areas and may affect global climate in the future. *Science (New York)*, *170*(3964), 1265–1274.

Landsberg, H. E. (1981). *The Urban Climate*. Academic Press.

Lo, C. P., Quattrochi, D. A., & Luvall, J. C. (1997). Application of high-resolution thermal infrared remote sensing and GIS to assess the urban heat island effect. *International Journal of Remote Sensing*.

Loughnan, M., Nicholls, N., & Tapper, N. (2010). Mortality-temperature thresholds for ten major population centres in rural Victoria, Australia. *Health and Place*, *16*(6), 1287–1290.

Mao, K., Shi. J.,an-cheng, Qin, Z., Gong, P., & Xu B. (2006). A Four-Channel Algorithm for Retrieving Land Surface Temperature and Emissivity from ASTER Data. *Journal of Remote Sensing*, *10*(4), 593–599.

Martin, P., Baudouin, Y., & Gachon, P. (2015). An alternative method to characterize the surface urban heat island. *International Journal of Biometeorology*, *59*(7), 849–61.

Memon, R. A., Leung, D. Y. C., & Liu, C. H. (2009). An investigation of urban heat island intensity (UHII) as an indicator of urban heating. *Atmospheric Research*, *94*(3), 491–500.

Mohsin, T., & Gough, W.A. (2014). Impact of climate change on the extremes of observed daily temperature data in the Greater Toronto Area. *International Journal of Climate Change: Impacts and Responses, 5*(1), 11-33.

Morgan, D., Myrup, L., Rogers, D., & Baskett, R. (1977). Microclimates Within an Urban Area∗. *Annals of the Association of American Geographers*, *67*(1), 55–65.

Morris, C. J. G., & Simmonds, I. (2000). Associations between varying magnitudes of the urban heat island and the synoptic climatology in Melbourne, Australia. *International Journal of Climatology*, *20*(15), 1931–1954.

Munn, R. E., Hirt, M. S., & Findlay, B. F. (1969). A Climatological Study of the Urban Temperature Anomaly in the Lakeshore Environment at Toronto. *Journal of Applied Meteorology*, *8*(3), 411–422.

Nichol, J.E. (1994). A GIS-based approach to microclimate monitoring in Singapore's high-rise housing estates. *Photogrammetric Engineering and Remote Sensing* 60: 1225–1232.

Nichol, J. E. (1996). High-Resolution Surface Temperature Patterns Related to Urban Morphology in a Tropical City: A Satellite-Based Study. *Journal of Applied Meteorology*.

Oke, T. R. (1973). City size and the urban heat island. *Atmospheric Environment Pergamon Press*, *7*, 769–779.

Oke, T. R. (1978). *Boundary Layer Climates*. New York: Wiley

Oke, T. R. (1982). The energetic basis of the urban heat island. *Quarterly Journal of the Royal Meteorological Society*, *108*(455), 1–24.

Oke, T. R. (1988). Street design and urban canopy layer climate. *Energy and Buildings*, *11*(1-3), 103–113.

Oke, T. R., & Maxwell, G. B. (1975). Urban heat island dynamics in Montreal and Vancouver. *Atmospheric Environment (1967)*, *9*(2), 191–200.

Park, H.-S. (1986). Features of the heat island in seoul and its surrounding cities. *Atmospheric Environment (1967)*, *20*(10), 1859–1866.

Payton, S., Lindsey, G., Wilson, J., Ottensmann, J. R., & Man, J. (2008). Valuing the benefits of the urban forest: a spatial hedonic approach. *Journal of Environmental Planning and Management*, *51*(6), 717–736.

Peng, S., Piao, S., Ciais, P., Friedlingstein, P., Ottle, C., Bréon, F.-M., … Myneni, R. B. (2012). Surface Urban Heat Island Across 419 Global Big Cities. *Environmental Science & Technology*, *46*(2), 696–703.

Qin, Z., Karnieli, a., & Berliner, P. (2001). A mono-window algorithm for retrieving land surface temperature from Landsat TM data and its application to the Israel-Egypt border region. *International Journal of Remote Sensing*, *22*(18), 3719–3746.

Rao, P. K. (1972). Remote Sensing of Urban Heat Islands from an Environmental Satellite. *Bulletin of American Meteorological Society*, 53, 647-648.

Rigo, G., & Parlow, E. (2007). Modelling the ground heat flux of an urban area using remote sensing data. *Theoretical and Applied Climatology*, *90*(3-4), 185–199.

Rinner, C., & Hussain, M. (2011). Toronto's urban heat island-exploring the relationship between land use and surface temperature. *Remote Sensing*, *3*(6), 1251–1265.

Rosenfeld, A. H., Akbari, H., Bretz, S., Fishman, B. L., Kurn, D. M., Sailor, D., & Taha, H. (1995). Mitigation of urban heat islands: materials, utility programs, updates. *Energy and Buildings*, *22*(3), 255–265.

Roth, M., Oke, T. R., & Emery, W. J. (1989). Satellite-derived urban heat islands from three coastal cities and the utilization of such data in urban climatology. *International Journal of Remote Sensing*, *10*(11), 1699–1720.

Rozenstein, O., Qin, Z., Derimian, Y., & Karnieli, A. (2014). Derivation of land surface temperature for landsat-8 TIRS using a split window algorithm. *Sensors (Switzerland)*, *14*(4), 5768–5780.

Runnalls, K. E., & Oke, T. R. (2000). Dynamics and controls of the near-surface heat island of vancouver, british columbia. *Physical Geography*, *21*(4), 283–304.

Sailor, D., & Hart, M. (2006). An Anthropogenic Heating Database for Major Us Cities. *86th AMS Annual Meeting.*

Sailor, D. J., & Fan, H. (2002). Modeling the diurnal variability of effective albedo for cities. *Atmospheric Environment*, *36*(4), 713–725.

Sailor, D. J., & Lu, L. (2004). A top-down methodology for developing diurnal and seasonal anthropogenic heating profiles for urban areas. *Atmospheric Environment*, *38*(17), 2737–2748.

Salamanca, F., Georgescu, M., Mahalov, a., Moustaoui, M., & Wang, M. (2014). Anthropogenic heating of the urban environment due to air conditioning. *Journal of Geophysical Research: Atmospheres*, *119*(10), 5949–5965.

Schmugge, T., Hook, S. J., & Coll, C. (1998). Recovering surface temperature and emissivity from thermal infrared multispectral data. *Remote Sensing of Environment*, *65*, 121–131.

Schneider, K., & Mauser, W. (1996). Processing and accuracy of Landsat Thematic Mapper data for lake surface temperature measurement. *International Journal of Remote Sensing*, *17*(11), 2027–2041.

Schott, J. R., & Volchok, W. J. (1985). Thematic Mapper thermal infrared calibration. *Photogrammetric Engineering & Remote Sensing*, *51*(9), 1351–1357.

Scott, R. W., & Huff, F. a. (1996). Impacts of the Great Lakes on Regional Climate Conditions. *Journal of Great Lakes Research*, *22*(4), 845–863.

Semenza, J. C., Rubin, C. H., Falter, K. H., Selanikio, J. D., Flanders, W. D., Howe, H. L., & Wilhelm, J. L. (1996). Heat-related deaths during the July 1995 heat wave in Chicago. *The New England Journal of Medicine*, *335*(2), 84–90.

Sen, P. K. (1968). Estimates of the Regression Coefficient Based on Kendall's Tau. *Journal of the American Statistical Association*, *63*(324), 1379–1389.

Smargiassi, A., Fournier, M., Griot, C., Baudouin, Y., & Kosatsky, T. (2008). Prediction of the indoor temperatures of an urban area with an in-time regression mapping approach. *Journal of Exposure Science & Environmental Epidemiology*, *18*(3), 282–288.

Sobrino, J. a., Jiménez-Muñoz, J. C., & Paolini, L. (2004). Land surface temperature retrieval from LANDSAT TM 5. *Remote Sensing of Environment*, *90*(4), 434–440.

Sobrino, J. a., Oltra-Carrió, R., Sòria, G., Jiménez-Muñoz, J. C., Franch, B., Hidalgo, V. Paganini, M. (2013). Evaluation of the surface urban heat island effect in the city of Madrid by thermal remote sensing. *International Journal of Remote Sensing*, *34*(9-10), 3177–3192.

Souch, C., & Grimmond, S. (2006). Applied climatology: urban climate. *Progress in Physical Geography*, *30*(2), 270–279.

Statistics Canada. (2011). *Table 051-0001 - Estimates of population, by age group and sex for July 1, Canada, provinces and territories, annual (persons unless otherwise noted),* CANSIM (database). Retrieved from http://cansim2.statcan.gc.ca/

Stewart, I., & Oke, T. R. (2009). Newly developed "thermal climate zones" for defining and measuring urban heat island "magnitude" in the canopy layer. *AMS Eighth Symposium on the Urban Environment*, January 11–15, Phoenix, AZ.

Stone, B. (2005). Urban Heat and Air Pollution: An Emerging Role for Planners in the Climate Change Debate. *Journal of the American Planning Association*, *71*(1), 13–25.

Stone, B. (2007). Urban and rural temperature trends in proximity to large US cities: 1951–2000. *International Journal of Climatology*, *27*(13), 1801–1807.

Taha, H. (1997). Urban climates and heat islands: albedo, evapotranspiration, and anthropogenic heat. *Energy and Buildings*, *25*(2), 99–103.

Taha, H., Konopacki, S., & Gabersek, S. (1999). Impacts of large-scale surface modifications on meteorological conditions and energy use: A 10-region modeling study. *Theoretical and Applied Climatology*, *62*(3-4), 175–185.

Tremeac, B., Bousquet, P., de Munck, C., Pigeon, G., Masson, V., Marchadier, C., … Meunier, F. (2012). Influence of air conditioning management on heat island in Paris air street temperatures. *Applied Energy*, *95*, 102–110.

Vincent, L. A., Wang, X. L., Milewska, E. J., Wan, H., Yang, F., & Swail, V. (2012). A second generation of homogenized Canadian monthly surface air temperature for climate trend analysis. J. Geophys. Res., 117, D18110.

Von Storch, H. (1995). Misuses of Statistical Analysis in Climate. *Analysis of Climate Variability: Applications of Statistical Techniques*, 11–26.

Von Storch, H., & Zwiers, F. W. (2003). *Statistical Analysis in Climate Research*. New York, NY, USA: Cambridge University Press

Voogt, J. a., & Oke, T. R. (2003). Thermal remote sensing of urban climates. *Remote Sensing of Environment*, *86*(3), 370–384.

Weng, Q., Lu, D., & Schubring, J. (2004). Estimation of land surface temperature-vegetation abundance relationship for urban heat island studies. *Remote Sensing of Environment*, *89*(4), 467–483.

Weng, Q., & Yang, S. (2006). Urban air pollution patterns, land use, and thermal landscape: An examination of the linkage using GIS. *Environmental Monitoring and Assessment*, *117*(1-3), 463–489.

Weng, Q. (2009). Thermal infrared remote sensing for urban climate and environmental studies: Methods, applications, and trends. *ISPRS Journal of Photogrammetry and Remote Sensing*, *64*(4), 335–344.

Whitman, S., Good, G., Donoghue, E. R., Benbow, N., Shou, W., & Mou, S. (1997). Mortality in Chicago attributed to the July 1995 heat wave. *American Journal of Public Health*, *87*(9), 1515–1518.

Xian, G., & Crane, M. (2006). An analysis of urban thermal characteristics and associated land cover in Tampa Bay and Las Vegas using Landsat satellite data. *Remote Sensing of Environment*, *104*(2), 147–156.

Xiao, R. B., Weng, Q. H., Ouyang, Z. Y., Li, W. F., Schienke, E. W., & Zhang, Z. M. (2008). Land surface temperature variation and major factors in Beijing, China. *Photogrammetric Engineering and Remote Sensing*, *74*(4), 451–461.

Yue, S., Pilon, P., Phinney, B., & Cavadias, G. (2002). The influence of autocorrelation on the ability to detect trend in hydrological series. *Hydrological Processes*, *16*(9), 1807–1829.

Yue, S., & Wang, C. Y. (2002). Power of the Mann-Whitney test for detecting a shift in median or mean of hydro-meteorological data. *Stochastic Environmental Research and Risk Assessment*, *16*(4), 307–323.

Zhang, X., Vincent, L. a., Hogg, W. D., & Niitsoo, A. (2000). Temperature and precipitation trends in Canada during the 20th century. *Atmosphere-Ocean*, *38*(3), 395–429.